Thermochronology of the highest Central Asian massifs (Khan Tengri -Pobedi, SE Kyrgyztan): evidence for Late Miocene (ca. 8 Ma) reactivation of Permian faults and insights into building the Tian Shan

Yann Rolland, Anthony Jourdon, Carole Petit, Nicolas Bellahsen, C. Loury, Edward R Sobel, Johannes Glodny

Thermochronology of the highest Central Asian massifs (Khan Tengri - Pobedi, SE Kyrgyztan): evidence for Late Miocene (ca. 8 Ma) reactivation of Permian faults and insights into building the Tian Shan

Rolland, Y.[a*], Jourdon, A.[b], Petit, C.[c], Bellahsen, N.[d], Loury, C.[c], Sobel, E.R.[e], Glodny, J.[f],

[a]*EDYTEM, Université de Savoie Mont-Blanc – CNRS, Le Bourget du Lac, France.*

[b]*CNRS, GET, Université Paul Sabatier, Toulouse, France.*

[c]*Université Côte d'Azur, CNRS, Géoazur, 250 rue Albert Einstein, Sophia Antipolis, France.*

[d]*Sorbonne Université, CNRS-INSU, Institut des Sciences de la Terre Paris, ISTeP UMR, Paris, France.*

[e]*Institut für Geowissenschaften, Universität Potsdam, Karl-Liebknecht-Str. 24-25, 14476 Potsdam, Germany.*

[f]*GFZ German Research Centre for Geosciences, Telegrafenberg, Building B, 14473 Potsdam, Germany.*

**corresponding author: yann.rolland@univ-smb.fr*

Keywords: $^{40}Ar/^{39}Ar$ dating, Apatite Helium dating, exhumation, tectonics, reactivation.

Abstract

Geological study of the Khan Tengri and Pobedi massifs highlights two phases of compressional fault displacements. A Late Permian/Triassic displacement phase is highlighted (1) by biotite $^{40}Ar/^{39}Ar$ ages of 265–256 Ma, suggestive of cooling of Pobedi mid-crustal granulites during >8 km of top-to-the-north motion of the Pobedi Thrust; (2) by $^{40}Ar/^{39}Ar$ dating of syn-kinematic phengite at 249–248 Ma, which suggests a crystallization age during top-to-the-south motion of the Khan Tengri Thrust shear zone; (3) by Apatite Helium (AHe) ages of 280-240 Ma on the crystalline basement below the Mesozoic peneplain, which gives insight into the final exhumation stage. Cenozoic reactivation of the Pobedi Thrust is indicated by AHe thermochronology with a mean age of 8.3 ± 2.5 Ma, in agreement with ~3 km exhumation and ~4.2 km of top-to-the-north motion in the Late Miocene. Along a north-south transect of the west Tian Shan range from Issyk-Kul Lake to Tarim Basin, compiled thermochronological data outline out-of-sequence deformation beginning with the activation of north-directed crustal-scale faults at 22-15 Ma along the northern margin of the north Tian Shan, followed by 20-10 Ma motion at the boundary between the Middle and the South Tian Shan, and ending with the <10 Ma reactivation of the Pobedi Thrust in the South Tian Shan. This latter coincided with south-directed motion on the South Tian Shan Front (the Maidan Fault) and fold and thrust belt propagation towards the Tarim Basin.

1. Introduction

Since the Early Cenozoic, deformation has propagated towards the core of the Eurasian continent in response to the India-Asia collision (e.g., Hu et al., 2016). Collisional deformation is now distributed over several thousand kilometres, from the Himalayan front to the interior of the Siberian craton (e.g. Avouac et al., 1993; Tapponnier et al., 1986; Sobel and Dumitru, 1997).

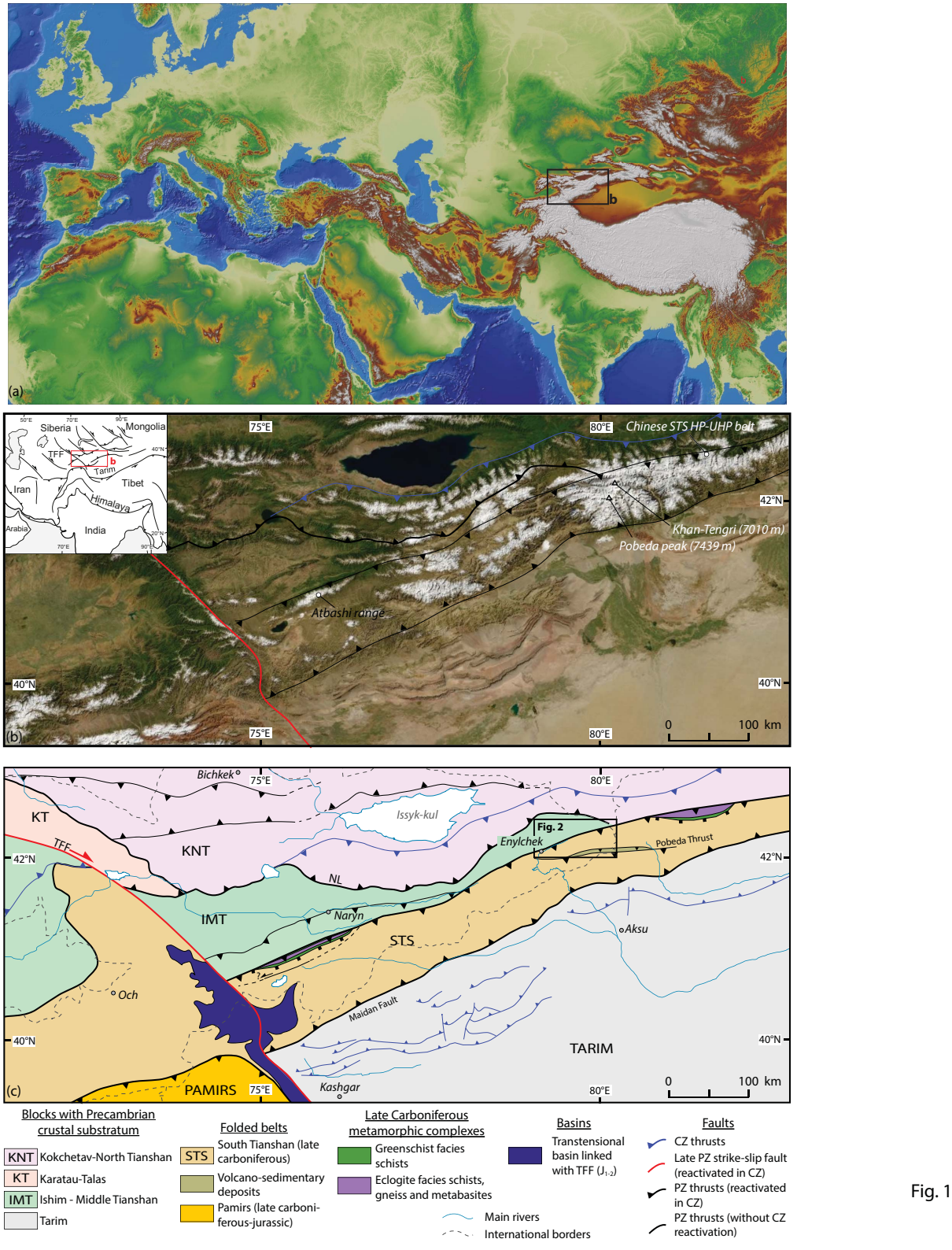

Fig. 1

Fig. 1. (a) Location of Tian Shan within the Alpine-Himalayan collisional system. (b) Satellite image of the Tian Shan belt showing study areas. Insert: geographical situation of Tian Shan in Central Asia (Map data: Google, Image Landsat). (c) Tectonic map of Tian Shan (Cenozoic cover removed). Location of detailed geological map of Fig. 2 is shown, modified after Loury et al. (2017). Abbreviations used: CZ, Cenozoic; TFF, Talas-Fergana Fault; NL, Nikolaev Line; STS, South Tian Shan; NTS, North Tian Shan.

This deformation has given rise to the highest intra-continental orogen, the Tian Shan mountain belt. The Tian Shan forms the south-western part of the Central Asian Orogenic Belt (CAOB; Fig. 1), extending for 2500 km from Uzbekistan to western China and was built up by successive continental accretionary events during the Palaeozoic (e.g. Sengör et al. 1993; Windley et al. 2007; Kröner et al. 2014; Loury et al., 2018b; Han et al., 2011). Active deformation occurs along crustal scale faults inherited from the (post) collisional evolution of the CAOB in Late Carboniferous to Permian times, which have been reactivated during the Cenozoic (e.g., Sobel et al. 2006b; Glorie et al. 2011; Macaulay et al. 2013, 2014; Loury et al., 2017, 2018a; Jourdon et al., 2018a-b; Rizza et al., 2019). Palaeozoic structures including collisional sutures and transcurrent shear zones of the CAOB have strongly localized Cenozoic deformation, while the domains between these faults behaved as rigid blocks (e.g., Jolivet et al., 2010; Glorie et al. 2011; Macaulay et al. 2013, 2014; Jourdon et al., 2018a-b). Prominent reactivation since the Neogene has resulted in the highest topography of Central Asia, with summits above 7000 m and large flat peneplains partly preserved from the Late Palaeozoic to Early Cenozoic erosional stages (e.g., Morin et al., 2019 and references therein). Cenozoic erosion is spatially variable, focussed on the highest ranges, while the formerly flat-lying Mesozoic peneplains are uplifted above 4000 m and form intra-orogenic plateaus (Jolivet, 2017; Morin et al., 2019). Reconstructing Cenozoic Tian Shan mountain building and comprehending active tectonics requires precisely locating the major faults, determining their crustal scale geometry and pin-pointing their activation throughout the Cenozoic with respect to the previous tectonic stages (e.g., Jourdon et al., 2018a-b). It is thus necessary to disentangle the relative contributions of the tectonic phases which affected the area since the Palaeozoic.

Previous works based on thermochronology and basin sedimentology along the Tian Shan belt have enabled quantifying several crustal compartments and along-belt uplift phases

(Jolivet et al., 2010, 2015, 2018; Glorie et al. 2010, 2011, 2019; De Grave et al., 2007, 2011, 2012, 2013, 2014; Macaulay et al., 2013, 2014; De Pelsmaeker et al., 2017; Yin et al., 2018; Zhao et al., 2019; Zhang et al., 2019). However, no such study was conducted in the highest part of the South Tian Shan (STS): the Pobedi and Khan Tengri massifs, which culminate above 7000 m. This most prominent Tian Shan topography is also a key zone to link the history of mountain building in the Kyrgyz western Tian Shan to the frontal fold and thrust belt and related foreland basin, the Tarim Basin, in NW China. For this, we have undertaken a geological, $^{40}Ar/^{39}Ar$ geochronological and apatite (U-Th-Sm)/He (AHe) thermochronological study. $^{40}Ar/^{39}Ar$ geochronology is applied to low-temperature mylonitic phengite in order to constrain the time of ductile (Palaeozoic?) deformation (e.g., Sanchez et al., 2011). AHe thermochronology is undertaken from underneath some major peneplains and on both sides of major thrusts to constrain the time of the final (Palaeozoic to Cenozoic) stages of exhumation. These data are integrated into a north-south crustal cross-section, and are used to reconstruct the deformation sequence which gave rise to the western Tian Shan belt.

2. Geological setting

The main tectonic units of the Tian Shan belt correspond to at least three continental blocks: the North Tian Shan (NTS), the Middle Tian Shan (MTS), the South Tian Shan (STS) - Tarim basin, separated by two Palaeozoic sutures: the Nikolaev Line (NL) and the STS suture (Figure 1; see a review of data in Loury et al., 2017). In China, the Yili-Central Tian Shan (YCTS) is equivalent to the Kyrgyz NTS. It is separated from the Chinese STS by the STS suture. The Kyrgyz MTS is not present in China (e.g., Jourdon et al., 2017). The main faults that reactivate the Kyrgyz Tian Shan suture zones are highlighted by geophysical (Makarov et al., 2010; Loury et al., 2017) and thermochronological data (De Grave et al., 2012; Macaulay et al., 2013; 2014; Glorie et al., 2010; 2011). Along the northern border of

103 the Tarim basin, seismic activity indicates top-to-the-south thrusting of the Tian Shan over the

104 Tarim basin, as also visible on the MANAS seismic profile (Makarov et al., 2010).

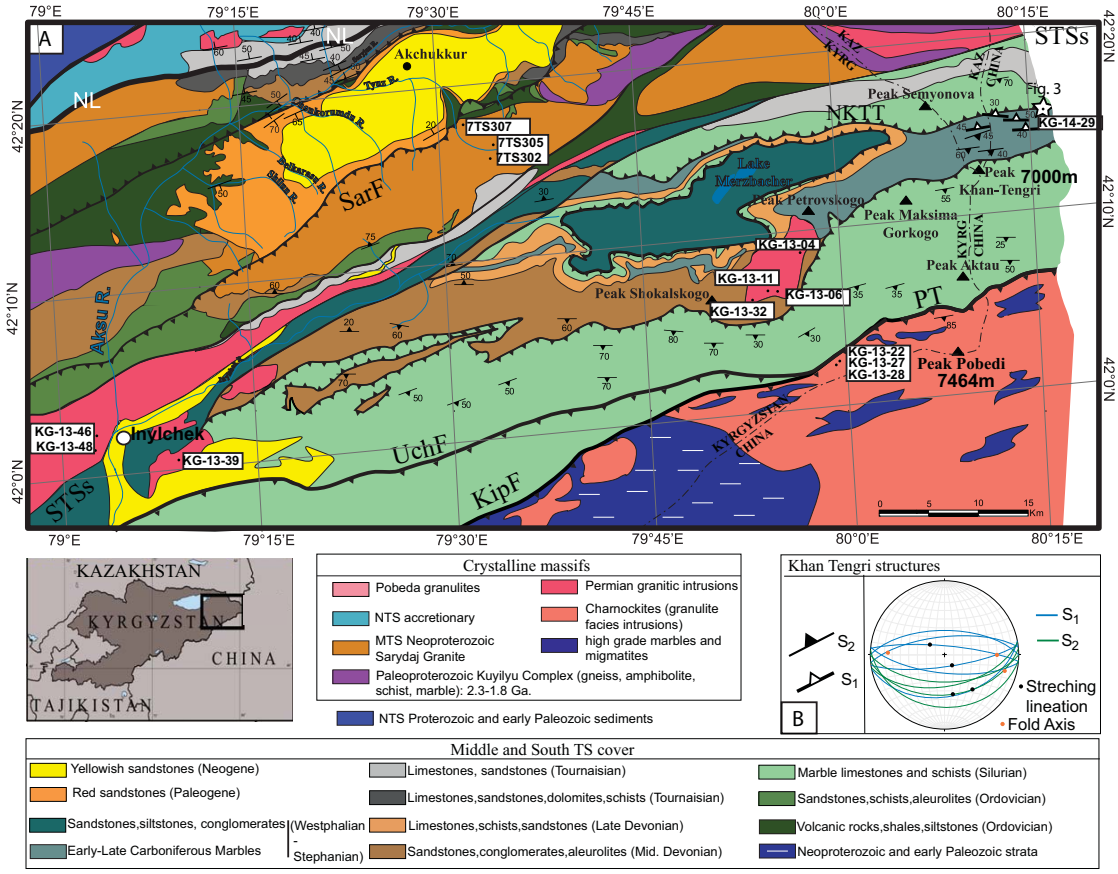

105

106 **Fig. 2.** A, Geological map of Inylchek-Khan Tengri-Pobedi area in Eastern Kyrgyz STS (modified after
107 Jourdon et al., 2017a, and Kröner et al., 2017). MTF: Main Terskey Fault; CTF: Central Terskey Fault; PT:
108 Pobedi Thrust; NKTT: North Khan Tengri Thrust; NL: Nikolaev Line; SarF: Sarajaz Fault; STSs: Southern Tian
109 Shan Suture; UchF: Uchchat Fault; KipF: Kipchak Fault. The location of dated samples is shown. Note also the
110 location of Fig. 3 pictures. B, Stereonet representing the structures measured to the north of Khan Tengri peak,
111 along the NKTT. Note that the two foliations (S1 and S2, see Fig. 3 pictures) strike E-W and bear a down-dip
112 lineation underlined by phengite (dated on Fig. 6), and gently dipping fold axes. These structural data can be
113 interpreted as representative of nearly pure N-S shortening along the NKTT.
114

115 The Pobedi and Khan Tengri massifs lie in SE Kyrgyzstan, in the STS domain (Figs. 1-2).

116 It is still unclear if the STS formed a distinct tectonic block or if it corresponds to the northern

117 margin of Tarim (see discussions in Loury et al., 2017; 2018b). The pre-Carboniferous

118 basement of the STS is unknown; sedimentary series belong to the Silurian to Carboniferous

119 periods (Tursungaziev and Petrov, 2008). These series are cross-cut by Late Carboniferous to

120 Early Permian granitoid intrusions and charnockite bodies, which were emplaced during the

Tarim-CAOB collisional to post-collisional transcurrent tectonic context. U/Pb ages on zircons from these granitoids range from 302 to 288 Ma (Konopelko et al., 2007; 2009; Glorie et al., 2011; Loury et al., 2018a). The MTS has a Palaeoproterozoic (2.3–1.8 Ga) basement, the Kuilyu Complex (Kröner et al., 2017). The STS suture was formed in the Late Carboniferous following the collision of the MTS and YCTS with the Tarim craton (Fig. 1; Loury et al., 2017; Jourdon et al, 2018a). This Carboniferous suture was then subjected to several phases of reactivation from (1) the post-collisional evolution of the CAOB in Permian times and (2) several moderate tectonic pulses in Mesozoic times to (3) the Cenozoic uplift of the belt.

2.1. Late Palaeozoic tectonic evolution of the STS

2.1.1. Formation of the belt during STS ocean subduction

Two distinct domains within the South Tian Shan belt, separated by 500 km along strike, expose High Pressure (HP) rocks, which have similar timing and pressure-temperature conditions: the Atbashi range in Kyrgyzstan and the Kebuerte-Kekesu area in China (e.g. Klemd et al., 2005; Simonov et al. 2008; Hegner et al. 2010; Su et al., 2010; Li et al., 2011; Loury et al., 2018b; Tan et al., 2019). The pressure-temperature-time data are consistent with the end of oceanic subduction in the STS and thus the onset of accretion or collision between Tarim and the CAOB at 315-320 Ma (Hegner et al. 2010, Loury et al., 2016, 2018b). In Kyrgyzstan, the structural and kinematic evolution related to this Late Carboniferous phase corresponds to an intense reactivation of the MTS-STS boundary in a overall transpressional context (Jourdon et al., 2017). In the western STS, nappe-stacking was expressed by top-to-the-north thrusts and top-to-the-south detachments in the Atbashi Massif between 330 and 310 Ma, resulting in the exhumation of a large high-pressure unit along the STS suture (Loury

et al., 2018b). To the east of the STS, a pristine (S1) top-to-the-south deformation phase is highlighted north of the Khan-Tengri massif (Jourdon et al., 2017, Fig. 3).

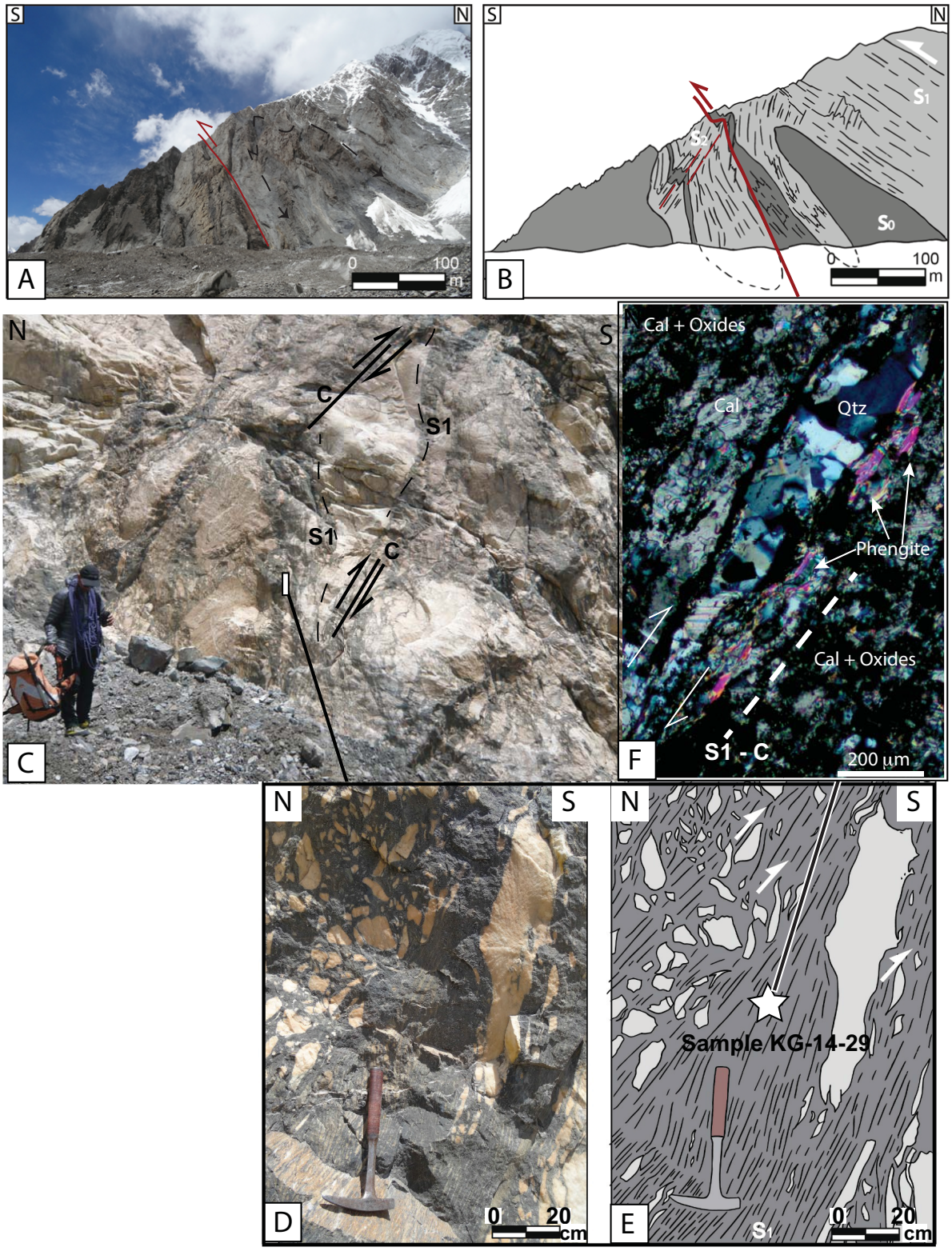

Fig. 3. Field photographs of the North Khan Tengri Thrust. A, View towards the NW and B, interpreted sketch, of the North Khan Tengri Thrust (NKTT). Major folding and thrusting together with S1 foliation are in agreement with top-to-the-south sense of shear. More local retro-deformation (S2, top-to-the-North) locally transects the S1 structures (see f.i., picture B). C, Picture of the central part of the NKTT shear zone with D-E, kinematic indicators and location of sample KG-14-29, showing top-to-the-south shearing (S1). F,

Microphotograph of sample KG-14-29 showing a sheared marble with abundant calcite (Cal) and oxides. Phengite occurs along elongate and sheared quartz (Qtz) layers. Phengite crystallized along the lineation and thus is synchronous with ductile deformation of the central shear zone of the North Khan Tengri Thrust. Phengite from sample KG-14-29 is dated by $^{40}Ar/^{39}Ar$;results are displayed in Fig. 6.

This phase was followed by S2 top-to-the-north thrusting, which cross-cuts the S1 structures. The most prominent S1 structure which we were able to sample in the field is the North Khan Tengri Thrust (NKTT; Figs. 2, 3). The timing of this tectonic transport is still unconstrained. To the south of Peak Khan Tengri, the top-to-the-north Pobedi Thrust (PT) transported the deep and high-grade (granulite facies) crystalline basement of the Pobedi range on top of the Devonian-Carboniferous low grade complex (Loury et al., 2018a; Figs. 4, 5).

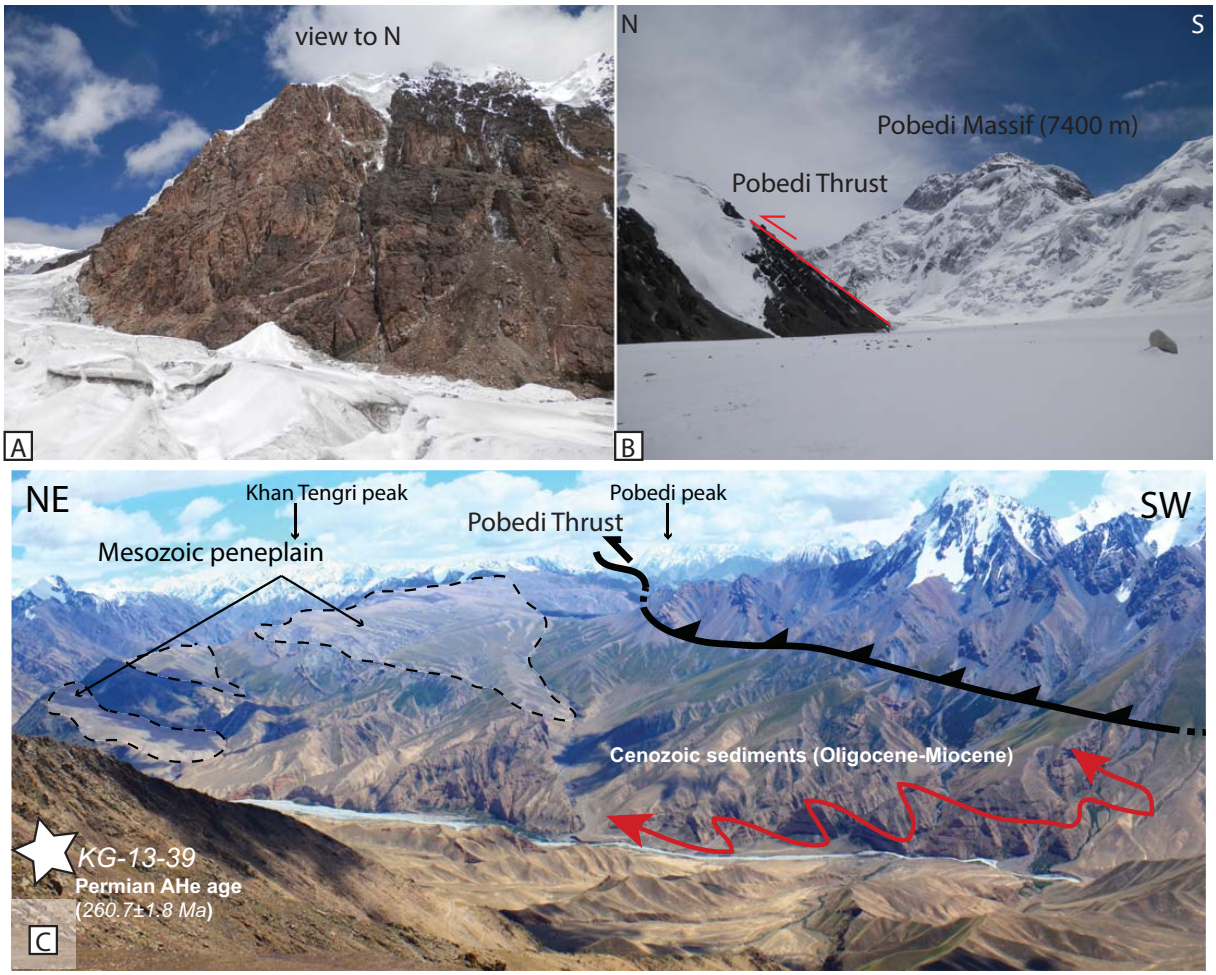

Fig. 4. Field photographs of the southern part of Kyrgyz STS. A, view of the southern flank of the '5539 m peak', showing an intrusive Permian granite cross-cutting the Devonian-Carboniferous low grade complex (schists, black shales, metagabbros). B, view towards the east of the Pobedi Thrust, which placed the high-grade (granulite facies) STS formation on top of the Devonian-Carboniferous low-grade complex. Location of photos is shown on Fig. 5. C, View towards the East showing the high Khan Tengri-Pobedi chain, from above Inylchek (location on Fig. 2). The Pobedi Thrust transports the southern STS onto the Mesozoic peneplain and the overlying Cenozoic basin.

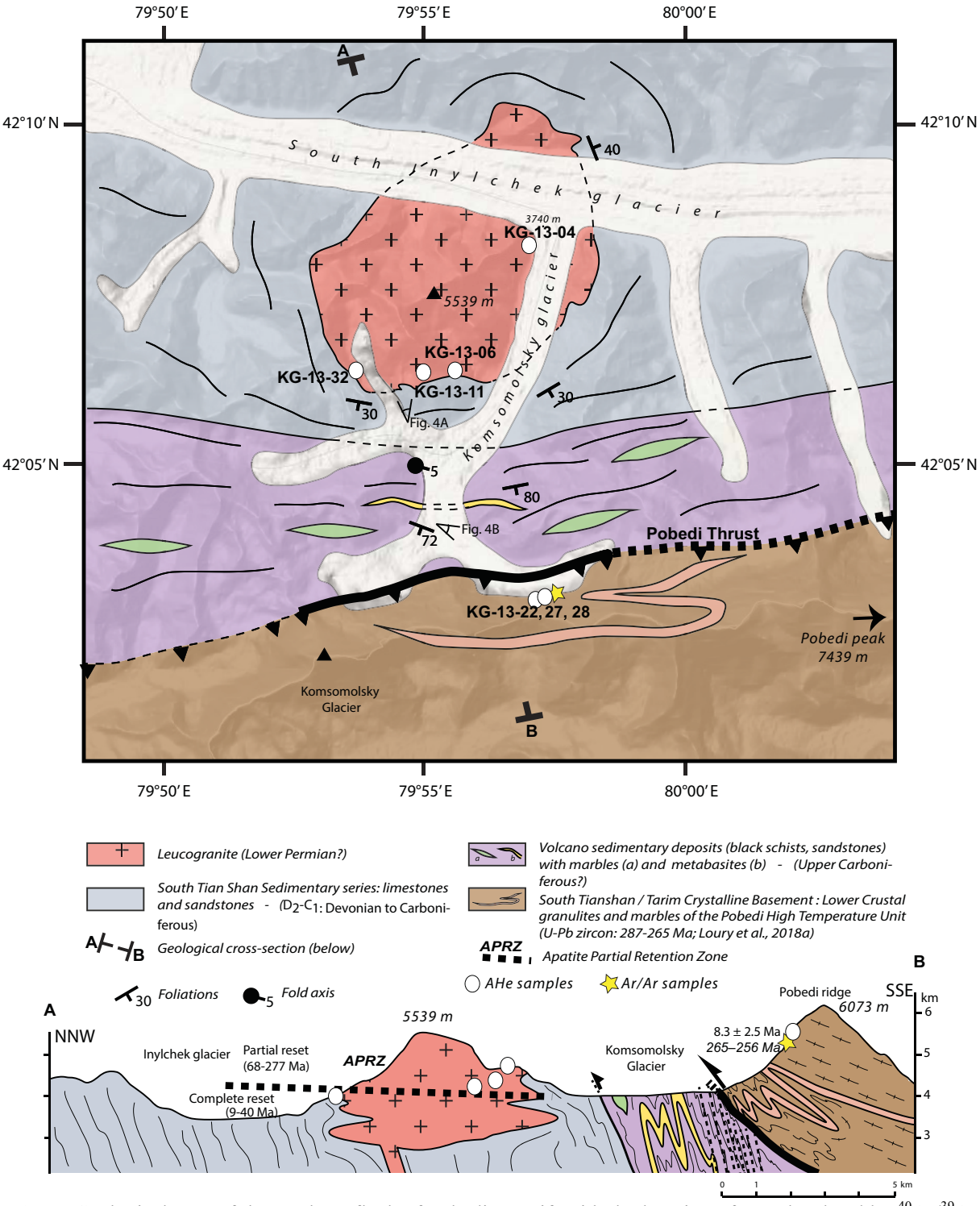

Fig. 5. Geological map of the northern flank of Pobedi Massif, with the location of samples dated by $^{40}Ar/^{39}Ar$ and AHe, and the position of the supposed lower limit of the apatite helium partial retention zone (see discussion). Position of pictures of Fig. 4 is also indicated.

The age of this tectonic transport is indirectly constrained by $^{40}Ar/^{39}Ar$ biotite ages between 265–256 Ma, which suggests a rapid cooling of the Pobedi granulites after the metamorphic

peak (287-265 Ma constrained by U-Pb on zircon and $^{40}Ar/^{39}Ar$ on amphibole; Loury et al., 2018a). Without any direct dating of deformation, it remains difficult to estimate which part of the thrust displacement is related to the Carboniferous/Permian and which could be related to Mesozoic or Cenozoic deformation events.

2.1.2. Post collisional evolution of the STS

After the last collisional phase that affected the CAOB in the Late Carboniferous, subduction continued to the south of the Tarim block (e.g., Metcalfe, 2013 and references therein). In the CAOB, a transition towards a transcurrent deformation regime along several roughly equally spaced NW-SE-trending large-scale faults occurred mostly in Permian times (e.g. the Talas Ferghana Fault or TFF in Kyrgyzstan and the Dzhungarian Fault in eastern Kazakhstan; Rolland et al. 2013; Konopelko et al. 2013). Sinistral strike-slip motion along the ENE-striking STS suture is supposed to be coeval to dextral strike-slip along the NW-striking TFF (Alekseev et al. 2007; Jourdon et al., 2017). The TFF was activated during the collision of Tarim with the Kazakh Platform at ca. 317 Ma, but remained active in Permian to Lower Jurassic times (Rolland et al. 2013; Konopelko et al. 2013; Morin et al., 2019), with up to 70 km of right-lateral slip in the Permian-Triassic (Alexeiev et al., 2017). During this phase of transcurrent deformation, the Tarim Basin experienced a significant phase of subsidence (Carroll et al. 1995). Intense magmatism affected the Tian Shan belt and northern Tarim during Early to Middle Permian times (290-260 Ma) (e.g. Biske et al., 2013; Chen et al., 1999, 2009; Li et al., 2011; Wang and Liu, 1991; Yang et al., 2006; Yu et al., 2011; Zhang et Zou, 2013). Magmatic emplacement is controlled by regional scale strike-slip faults (e.g. de Jong et al., 2009; Shu et al., 1999; Wang et al., 2007; 2009; 2014; Loury et al., 2018a); the source of these alkaline OIB-like magmatic rocks (e.g. Zhang et Zou, 2013; Zhou et al., 2009)

205 is ascribed to mantle plume activity (e.g. Yang et al., 2005, 2006, 2013, Yu et al., 2011; Biske
206 et al. 2013; Loury et al., 2018a).
207
208 *2.2. Mesozoic reactivation of the STS*
209 Mesozoic transcurrent tectonic activity along the TFF is evidenced by Late Triassic to Early
210 Jurassic $^{40}Ar/^{39}Ar$ ages (Rolland et al. 2013; Konopelko et al. 2013). This brittle reactivation
211 occurred in a transtensional regime, and resulted in pull-apart basins with up to 70 km of right
212 lateral slip in the Jurassic (Alexeiev et al., 2017). Furthermore, sedimentary deposits and
213 thermochronological data suggest that at least one and up to three exhumation stages occurred
214 in the Tian Shan during the Mesozoic (e.g. De Grave et al., 2007, 2011, 2013, 2012; Dumitru
215 et al., 2001; Glorie et al., 2011; Hendrix, 2000; Hendrix et al., 1992; Jolivet et al., 2010;
216 Macaulay et al., 2014).
217 A first exhumation stage of the STS during the Late Jurassic at ca. 160–145 Ma is suggested
218 based on Apatite Fission Track (AFT) and apatite or zircon (U-Th)/He ages (Hendrix et al.,
219 1992; Dumitru et al., 2001; De Grave et al., 2007, 2013; Glorie et al., 2011; Jolivet et al.,
220 2010; Chang et al., 2019). This event is also emphasized by a major alluvial conglomerate in
221 the sedimentary record of the Tarim, Turpan and Junggar basins (Hendrix, 2000; Hendrix et
222 al., 1992; Li et al., 2004; Jolivet et al., 2013), and is possibly related to collisional processes
223 along the southern boundary of Eurasia, such as the accretion of the Lhasa block to the
224 Eurasian margin (e.g. Hendrix et al., 1992; Yin and Harrison, 2000; Yang et al., 2017).
225 In the Late Jurassic-Early Cretaceous, a period of thermal stability is well-documented, with
226 cooling rates lower than 1°C/Myr (e.g. Bullen et al., 2003, 2001; Jolivet et al., 2010;
227 Macaulay et al., 2014). This long period of tectonic quiescence is also supported by the
228 formation of large peneplains and alluvial fans in western Central Asia (Hendrix et al., 1992;

Dumitru et al., 2001; Jolivet et al., 2007, 2009, 2015; Vassallo et al., 2007; Jolivet, 2015; Morin et al., 2019).

A second pulse of Tian Shan exhumation in the Late Jurassic/Early-Mid Cretaceous is emphasized by numerous AFT ages, which are concentrated around ~120–95 Ma (Glorie and De Grave, 2016). This event, or slow cooling between significant events, corresponds with a major hiatus in the sedimentary record of the Tarim Basin (e.g., Dumitru et al., 2001 and references therein).

Several studies (De Grave et al., 2007, 2011, 2012, 2013; Glorie et al., 2011; Hendrix et al., 1992; Jolivet et al., 2010) suggest that a third and last Mesozoic Tian Shan exhumation phase occurred during the Late Cretaceous-Early Paleogene at ~75–60 Ma. Indeed, AFT and (U-Th)/He ages are obtained for this time range in the Narat and Bohoro ranges of Chinese Tian Shan (Jolivet et al., 2010), and especially in the southern part of CAOB (Gillespie et al., 2017). In Kyrgyzstan, similar ages are obtained from intrusions bordering the south Tian Shan suture (Glorie et al., 2011), in the Song-Kul plateau (De Grave et al., 2011), in the Issyk-Kul basement (De Grave et al., 2013), in the Altai mountains (De Grave et al., 2012) and in Central STS (Macaulay et al., 2014). However, these ages could clearly correspond to partially reset ages Macaulay et al. (2014), and may have no geological significance. Several tectonic events occurred during this time range, such as Kohistan-Ladakh arc accretion to Eurasia (Rolland et al., 2000; De Grave et al., 2007; Hendrix et al., 1992; Jolivet et al., 2010) and the collision of Siberia with the Mongolia-North China Block following the closure of the Mongol-Okhotsk Ocean (e.g. Jolivet et al., 2010; Lin et al., 2008; Metelkin et al., 2007); cooling within the Tian Shan has been correlated with these events (REFS).

252 *2.3. Cenozoic reactivation of the STS*

253 Little exhumation occurred in the Cenozoic until the Early Miocene (e.g., Jolivet et al., 2018).
254 A period of renewed cooling is highlighted by widespread AFT, ZHe, AHe Early Palaeogene
255 ages (ca. 55–45 Ma; see Glorie and De Grave, 2016 for a review), or might again reflect
256 some partial age resetting, as suggested by Macaulay et al. (2014). This potential event occurs
257 at the scale of the Tian Shan belt (Jolivet et al., 2010). These cooling ages are only found in
258 close proximity to major fault zones, which suggests that Palaeogene resetting or cooling is
259 mainly controlled by fault reactivations. However, this phase resulted in minor exhumation as
260 Late Palaeozoic and Mesozoic exhumation ages are widely preserved. This transient
261 deformation phase could be attributed to the onset of India-Asia collision (e.g., Hu et al.,
262 2016).

263 In the Kyrgyz Tian Shan, it is suggested that the onset of the modern orogeny occurred during
264 the Early Miocene (~30–22 Ma) with an apparent intensification in the Late Miocene (~12–8
265 Ma) and in the Plio–Pleistocene (<5 Ma; see for Macaulay et al., 2014 for a review). There,
266 Cenozoic exhumation is clearly documented since the Oligocene around 25-20 Ma (Hendrix
267 et al., 1994; Sobel et Dumitru, 1997; Yin et al., 1998; Bullen et al., 2001; Sobel et al., 2006a-
268 b; Heermance et al., 2008; De Grave et al., 2007, 2011; Glorie et al., 2010, 2011; Macaulay et
269 al., 2014, 2013; Glorie and De Grave, 2016; Bande et al., 2017). The onset of exhumation is
270 linked to a progressive transfer of compressional stresses of India-Asia collision into the
271 Asian continent (e.g., Molnar et Tapponnier, 1975) after the closure of marginal basins and a
272 significant thickening of the Himalayan collision zone. Diffuse regional exhumation was
273 likely followed by focussed exhumation due to the activation of major thrusts in relation to a
274 soft to hard collision of India with Eurasia (Heermance et al., 2007; Glorie and De Grave,
275 2016). In parts of the Tian Shan, Cenozoic deformation was out-of-sequence (Jolivet et al.,
276 2010; Macaulay et al., 2014), with a significant lateral variation along major reactivated

277 structures. This out-of-sequence activation could be explained by the dip and nature of the
278 inherited structures that were more or less susceptible to reactivation (e.g. Macaulay et al.,
279 2014; Jourdon et al., 2018a). To the north, the NTS basement over-thrusts the Issyk-Kul
280 Cenozoic basin along the Main Terskey Fault (MTF) (Macaulay et al., 2013).
281 Thermochronological data show that this structure was activated during the Late Oligocene
282 (~25 Ma ago) and propagated eastward during the Miocene (Macaulay et al., 2013). In the
283 central part of the belt, the STS suture was reactivated by a top-to-the-north thrust, which
284 uplifted the STS units over the MTS from 20 to 8 Ma (Macaulay et al., 2014; Glorie et al.,
285 2011). An increase in exhumation rates occurred during Miocene times (12-8 Ma and <5 Ma),
286 as documented by abundant thermochronological data (e.g. Bullen et al., 2001; 2003; De
287 Grave et al., 2007, 2011; Glorie et al., 2010, 2011; Macaulay et al., 2014, 2013; Sobel et al.,
288 2006b). The exhumation rate is estimated at 0.1–0.4 mm/yr in the Terskey Range of the NTS
289 during the Miocene (Macaulay et al., 2013). Acceleration of tectonic uplift and erosion are
290 also suggested by magnetostratigraphic data and sedimentary records in the Tarim foreland
291 Basin (e.g. Abdrakhmatov et al., 1996; Charreau et al., 2006; Heermance et al., 2007, 2008;
292 Chang et al., 2012, 2017). An increase in deformation and the activation of new faults in the
293 Tian Shan range since ca. 12 Ma may explain the anomalously high topography in the
294 southern Tian Shan, particularly summits above 7400 m in the Pobedi and Khan Tengri
295 massifs. However, data have not yet been reported from the highest mountains within the Tian
296 Shan in order to relate its formation to the rest of the belt.
297

298 ## 3. Methods and dating results

299 ### *3.1. $^{40}Ar/^{39}Ar$ dating*

300 #### 3.1.1. Analytical methods

In order to constrain the tectonic and cooling history of the STS basement in eastern Kyrgyzstan, $^{40}Ar/^{39}Ar$ dating was performed on a marble mylonite (sample KG-14-29) of the North Khan Tengri Thrust (NKTT; Figs. 2-3) to provide an age constraint for tectonic motion on this thrust. Sample KG-14-29 was crushed to a size fraction of 500-800 µm and cleaned in an ultrasonic bath. Phengites were carefully handpicked under a binocular microscope to select only grains without evidence of alteration or inclusions. Phengite aggregates from elongated syn-kinematic pressure-shadows were less than 800 µm in size (Fig. 3F). Selected grains and aggregates were packed in aluminum foil and irradiated for 40 hours in the Triga Mark II nuclear reactor of Pavia University in Italy together with Fish Canyon sanidine grains as flux monitor (28.03 ± 0.08 Ma, Jourdan and Renne, 2007). For this reactor, the following correction factors for argon nuclear interferences were applied after irradiation of pure salts of KF and CaF_2: $(^{36}Ar/^{37}Ar)_{Ca}$= 0.000288 ± 0.000016 ; $(^{39}Ar/^{37}Ar)_{Ca}$= 0.000727 ± 0.000041; $(^{40}Ar/^{39}Ar)_{k}$= 0.00969 ± 0.00038; $(^{38}Ar/^{39}Ar)_{k}$= 0.01297 ± 0.00045. All samples were analyzed by single-grain infrared CO_2 laser fusion analysis, and isotopic ratios were measured using an ARGUS VI multi-collector mass spectrometer at Geoazur institute of the University of Nice. System blanks were measured every three experiments. Mass discrimination for the mass spectrometer was monitored by regularly analyzing air pipette volumes. The ArArCalc © software v2.5.2 was used for data processing. Decay constants are those given by Steiger and Jäger (1977). Uncertainties on apparent and plateau ages are given at the 1σ level including the error on the $^{40}Ar^*/^{39}Ar_k$ ratio of the monitor. The criteria we used for defining a plateau age are: (1) it should contain at least 70% of total ^{39}Ar released, (2) it should contain at least three successive step-heating fractions, (3) the integrated age of the plateau, calculated by a weighted average of apparent ages of individual fractions comprising the plateau, should be consistent with each apparent age of the plateau within a 2σ error. A detailed table of results is given in Table 1.

3.1.2. Marble mylonite (sample KG-14-29) phengite $^{40}Ar/^{39}Ar$ dating results

4 phengite aggregates from the KG-14-29 marble mylonite were analyzed and results are presented in Fig. 6 and Table 1.

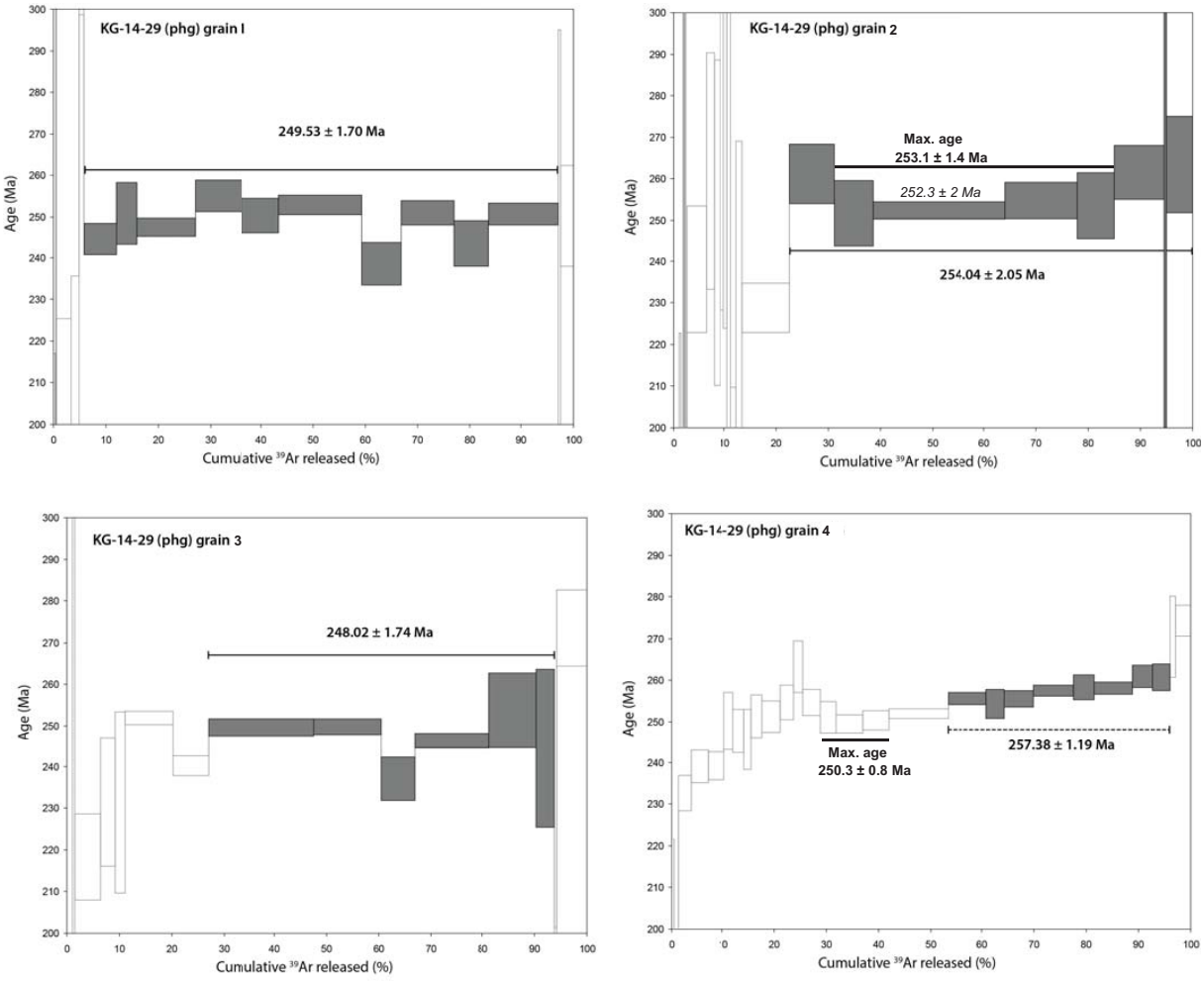

Fig. 6. North Khan Tengri Thrust shear zone mylonite sample KG-14-29 $^{40}Ar/^{39}Ar$ phengite dating results. The location, field relationships and petrological features of the dated sample are shown in Figs. 2-3.

Aggregate 1 yields a well-defined plateau age of 249.5 ± 1.7 Ma (MSWD = 1.44) including 10 steps and 91% of ^{39}Ar released. An inverse isochron age of 251.6 ± 1.6 Ma (MSWD = 1.58) is calculated, which is consistent within errors with the plateau age. Aggregate 2 shows a more disturbed spectrum in the low-temperature steps, which might represent some outer grain alteration. At higher temperatures, a plateau age is obtained at 254.0 ± 2.1 Ma (MSWD = 0.54), corresponding to 77% of ^{39}Ar released in 8 steps. However, its slight "U" shape

might be indicative of some (relatively minor) excess argon (e.g., Arnaud and Kelley, 1995), so the central part of the spectra might be regarded as a maximum age (253.1 ± 1.4 Ma with the central four steps or 252.3 ± 2 Ma with the lower central one).

Aggregate 3 shows a pattern with increasing apparent ages for the low-temperature steps. Then a plateau age of 248.0 ± 1.7 Ma (MSWD = 1.45) is obtained, including 6 steps and 67% of released ^{39}Ar.

Finally, the last phengite aggregate (Aggregate 4) shows a staircased shape with apparent ages continuously increasing. A pseudoplateau age is obtained for high-temperature steps (19 to 26) of 257.4 ± 1.2 Ma (MSWD = 1.00), including 44% of ^{39}Ar released in 9 steps. However, this age is not considered geologically meaningful because (i) this part of the spectra is not flat and shows a steady increase from 255 to 261 Ma, and (ii) the last two steps increase significantly up to 274 Ma. Therefore, it seems that this part of the spectra is influenced by some inherited argon released in the higher temperature steps, which may be hosted in mineral inclusions such as epidote or titanite (e.g., Simon-Labric et al., 2009) in the grain core. If we retain the hypothesis of some (relatively minor) inherited argon in this sample, then the central portion of the spectra is the closest to the crystallization age (and thus represents a maximum age) of 250.3 ± 0.8 Ma, which is similar within error to the three other ages.

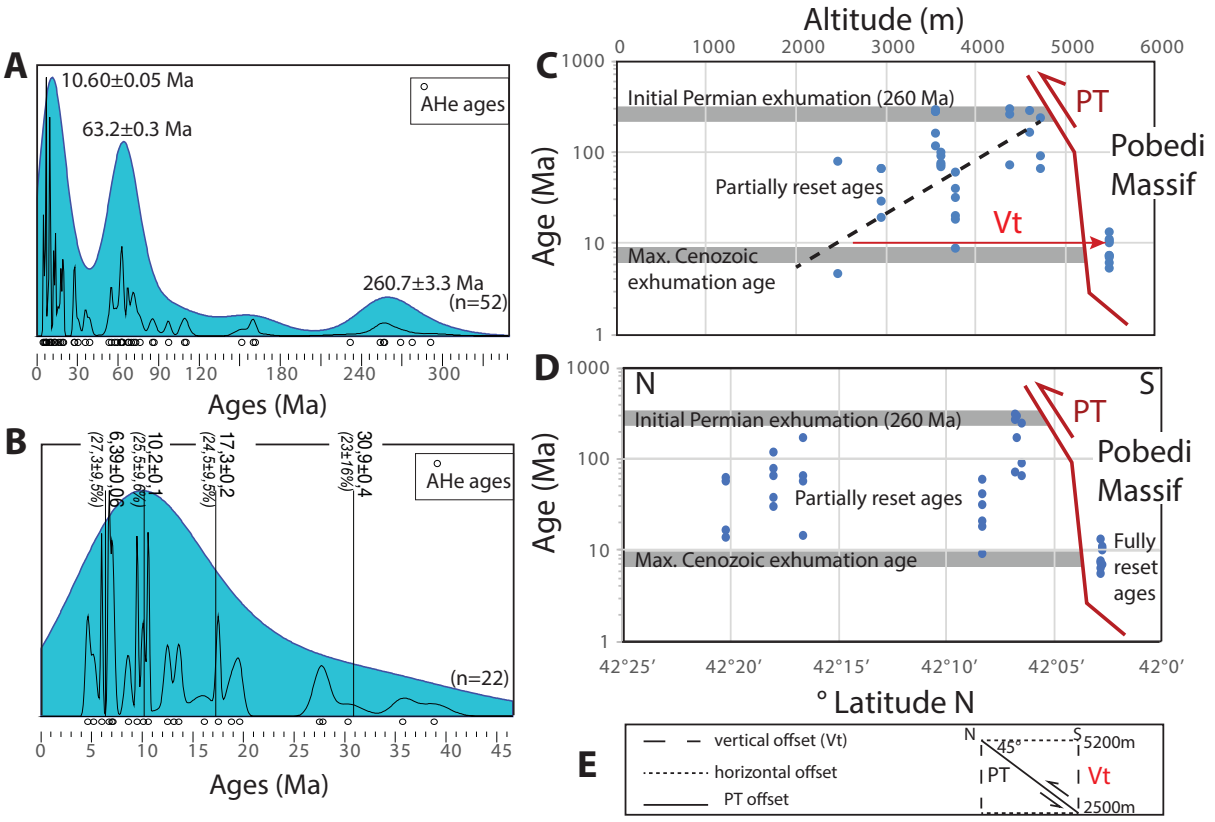

Fig. 7. Distribution of obtained AHe in this paper. A, Plot of all obtained AHe dates in this study, which shows a broad trimodal distribution, with Permian (260±5 Ma), Late Mesozoic-Early Cenozoic (~63.2 Ma), and Miocene (~10.6 Ma) peaks. This plot shows the spread in the obtained AHe dates, which are not all considered to be geologically meaningful (some of the ages are explained by partial resetting and inheritance, see the text for details). B, enlargement of the 0-50 Ma time range, which displays the equal weight of four age peaks in the age distribution at 6.4, 10.2, 17.3 and 30.9 Ma. C, Distribution of ages versus altitude along STS (including the Naryntoo Range). D, Distribution of ages versus latitude of samples of the Khan Tengri-Pobedi massifs. In the Pobedi Thrust (PT) footwall domain, the minimum age of the Late Palaeozoic exhumation is constrained by the older AHe ages, while the maximum age of the Cenozoic exhumation is constrained by the younger ages. The spread between these two ages is interpreted to reflect partial resetting of the apatite helium system during the Cenozoic. Vt represents the minimum vertical offset deduced for the Pobedi Thrust (PT) at ca. 8-10 Ma rocks. E, sketch of relative offsets on the PT inferred from Vt and the 45° dip of the thrust.

3.2. U-Th-Sm/He ages of Apatites

3.2.1. Strategy & Methodology

13 new apatite samples have been analyzed by U-Th-Sm/He (AHe) in this study. Samples were gathered from Palaeozoic basement lithologies from the STS, from the highest Pobedi Massif in the east (from which no thermochronological data has previously been published) to the flat region of the STS uplifted peneplain. These data are combined with published data (Glorie et al., 2011; De Grave et al., 2013; 2014; Macaulay et al., 2013; 2014). In this work,

AHe analyses were conducted on two to six single crystal aliquots per sample, depending on sample quality (Table 2). Apatite grains were extracted using standard mineral separation techniques and packed in platinum tubes for U, Th, Sm, and He isotopic analysis at the University of Potsdam and GFZ German Research Centre for Geosciences, Potsdam, Germany. Average AHe ages of Durango apatite standards analyzed were 29.1±1.1, 30.7±2.4, and 29.0±0.8, which are comparable to published averages of replicate analysis (e.g., 31.0 ± 1.0 and 32.1 ± 1.1 Ma; McDowell et al., 2005; Min et al., 2006). The Ft correction factor is calculated using the grain size (e.g., Farley, 2002). Any aliquot differing by more than 75% from the mean value of the other aliquots of a given sample was considered erroneous and was thus discarded from the data set. The 2 sigma standard error is representative of the uncertainties associated with the method and the natural reproducibility of the AHe system than the analytical error on individual aliquots. For more details on the methodology used for AHe dating, the reader is referred to Zhou et al. (2017).

3.2.2. AHe dating results

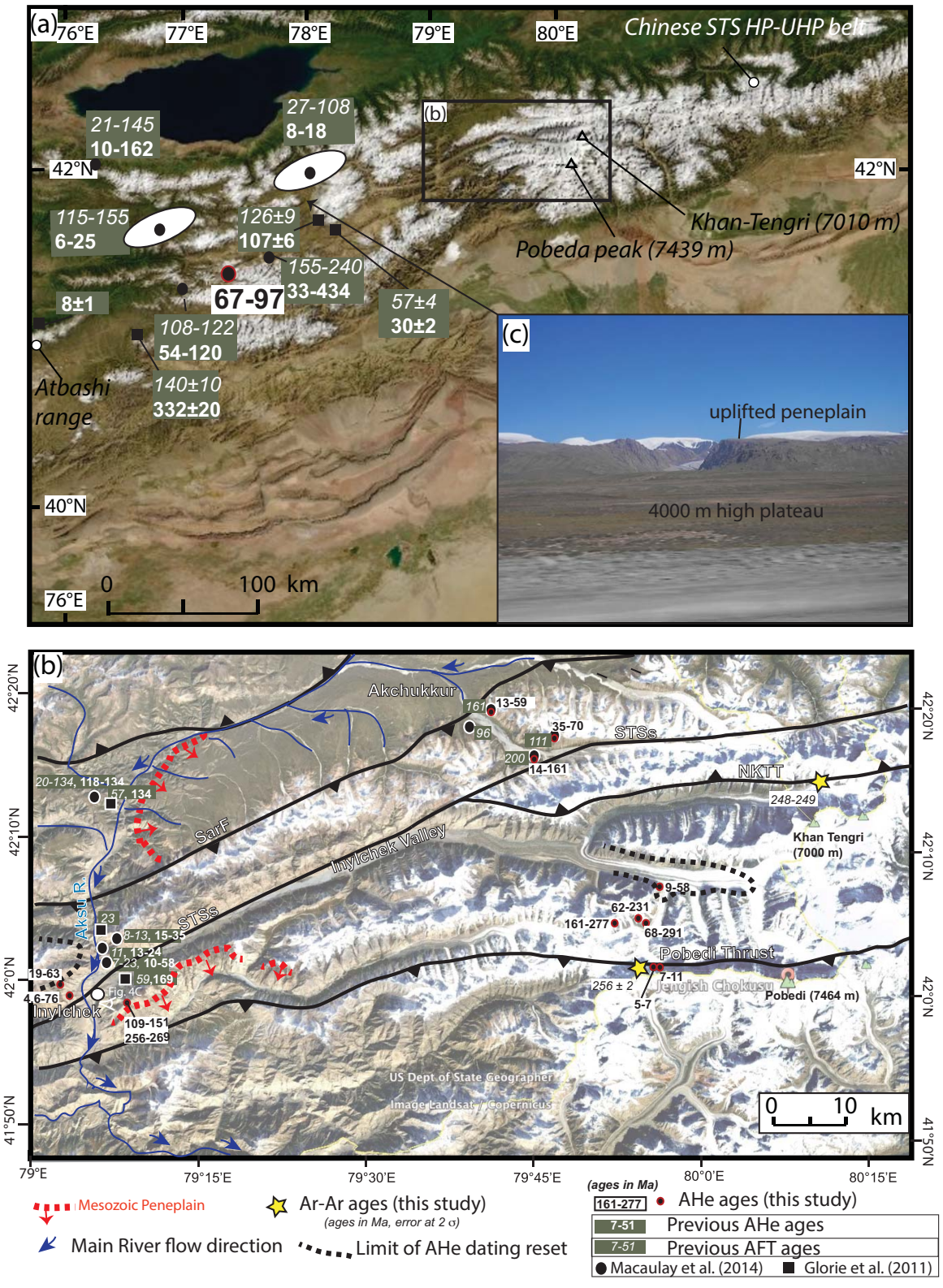

Fig. 8. Satellite image showing the AHe dating results obtained in the STS. A, Results of dating in the Naryn River area. B, Results obtained in the Pobedi - Khan Tengri - Pobedi area. AHe and AFT data from the literature are also shown.

399 AHe results are displayed in Table 2 and the main results are shown in Figs. 8-9. Most of our
400 AHe samples yielded over-dispersed single crystal aliquot ages. Such AHe age variability
401 may be related to differences in the diffusion characteristics between aliquots caused by grain
402 size variations, radiation damage, or the number of intact crystal terminations (e.g., Farley,
403 2000; Reiners et al., 2004; Flowers et al., 2009; Brown et al., 2013), and to subsequent
404 incomplete resetting due to burial within the apatite partial retention zone (e.g., Macaulay et
405 al., 2013, 2014). Therefore, variations in AHe ages within a given sample could be accurate
406 and potentially provide informations about its thermal history. Plotting age versus Ft (Suppl.
407 Fig. 1) shows that KG-13-48 and KG-13-11 and possibly KG-13-27 may have a positive
408 relationship between closure temperature and grain size. There are no obvious relationships
409 between age and eU (Suppl. Fig. 1); however, aliquots of samples KG-13-27 and -28 have
410 extremely high eU values and therefore may have anomalously high closure temperatures.
411 Alternatively, erroneous ages can reflect inclusions, (healed/unhealed) fractures, ^{4}He
412 implantation and U-Th(-Sm) zonation (e.g., Farley, 2002; Dobson et al., 2008; Macaulay et
413 al., 2014).
414 Significant variations are observed in the spread of thermochronological ages obtained in our
415 samples from different parts of the STS, which mainly relate to their structural situation
416 within the study area (Fig. 8). These variations are considered to be significant in the light of
417 previous data and of this structural situation. Four different geochronological configurations
418 can be inferred from the distribution of AHe ages:
419 - (i) in zones lying directly below the Mesozoic peneplain:
420 In the central STS, in the Naryntoo Range (sample KG13-78, Fig. 8A), all aliquots are
421 spread within 18% of the average age, and thus an average age of ca. 78 Ma is
422 retained for this sample, which is considered as geologically meaningful. This age

could correspond to cooling of the sample below ca. 60°C (e.g., Farley, 2002). We relate this age to a period of slow erosion during formation of the erosion surface.

South of Inylchek (Fig. 8B), sample KG13-39 presents three aliquot ages of 256-269 Ma, and two aliquots of 109 and151 Ma. The group of three Late Permian aliquots is close to the granite protolith U-Pb age of 285-305 Ma obtained by Konopelko et al. (2007). These granites must have been emplaced at a very shallow level as they intrude low grade schists (Loury et al., 2018a), and therefore the 256-269 Ma AHe ages are considered to be geologically meaningful. Both <200 Ma AHe aliquots have two broken ends and therefore the Ft correction may be less precise; therefore, we discard these two ages.

- (ii) To the north of the STS suture, north of Inylchek village (Fig. 8B), Cenozoic ages are obtained in samples KG13-46 & 48, in agreement with previous datings by Glorie et al. (2011) and Macaulay et al. (2014). However, there is a large spread in ages from 4.6 to 63 Ma, which also reflects the spread in ages of previous studies in the same area. For sample KG13-48, the age spread may reflect a Ft relationship. These dispersed ages could suggest that this zone has remained within the helium partial retention zone after a mid-Cenozoic phase of uplift initiated at > 19 Ma (Macaulay et al., 2014), with a possible increase of exhumation after 10 Ma.
- (iii) in the high Pobedi-Khan Tengri massifs (Fig. 8B), two different zones have been dated, which both record incomplete Cenozoic resetting. In this domain, the AHe data are dispersed which is ascribed to an incomplete reset of this chronometer: (1) to the north, SE of Akchukkur basin, in the hanging wall compartment of the NKTT and SarF, two samples (7TS302 and 305), from elevations of 3818 and 3540 m, respectively, show a spread of ages between 13 and 160 Ma, which is in agreement with incomplete resetting during the Cenozoic tectonic phase. It is also compatible

with monotonic slow cooling, as modeled by Macaulay et al (2014, Fig. S3). Sample 7TS307, which comes from the direct vicinity of SarF at a lower elevation of 3200 m, was strongly reset during the Cenozoic and gives ages of 13 to 59 Ma. However, the large amount of single aliquot dispersion argues for prolonged residence within the apatite partial retention zone. (2) The second sampled zone lies in the footwall compartment of the PT. Samples KG13-04, 06, 11, and 32 were collected along Inylchek Glacier, at high elevations (3790-4800m) on the northern flank of Peak Pobedi. These samples display a high variation in ages, ranging from 9 to 291 Ma. Many of these aliquots have extremely low eU values, suggesting that these results may be less reliable; however, all aliquots which yielded Cenozoic ages have higher eU values. For samples above 4000 m, all ages lie between the Permian and the Cenozoic (291-62 Ma). Only sample KG13-04, collected at 3785 m, displays Cenozoic ages (58-9 Ma). We interpret the age pattern of samples collected between 4000 and 4800 m as reflecting partial resetting of AHe ages within the apatite partial retention zone due to underthrusting and hence reheating (Jourdon et al., 2018a-b), as this zone corresponds to the footwall compartment of the PFT thrust and also exhibits a thick Cenozoic cover south of Inylchek (Fig. 4C).

- (iv) In the hanging-wall part of the Pobedi Thrust, at an elevation > 5500 m, samples KG13-27 & 28 display a narrow age variation within 5.2-12.5 Ma, which is considered geologically meaningful. Two average ages could be calculated, of 7.6 ± 1.8 Ma for KG13-27, and 9.2 ± 2.9 Ma for KG13-28, or 8.3 ± 2.5 Ma combining the two samples, which are very near from each other. As compared to the footwall compartment of Pobedi Thrust, which has an incompletely reset AHe age, we interpret this 8.3 ± 2.5 Ma age as resulting from the significant differential exhumation of the two compartments in response to the PT activation at <10 Ma.

4. Discussion

4.1. Tectonic significance of the Permian $^{40}Ar/^{39}Ar$ and AHe ages

$^{40}Ar/^{39}Ar$ dating on phengite of the Khan-Tengri Thrust mylonitic marble provides chronologic constraints on an episode of compressional tectonics within the STS belt in the Late Permian - Early Triassic. The $^{40}Ar/^{39}Ar$ technique has been widely used to date deformation-induced neo-crystallized K-white mica (e.g. Dunlap, 1997; Rolland et al., 2008; 2013; Sanchez et al., 2011; West et Lux, 1993). In this paper (section 3.1 and Fig. 6), four phengite aggregates yield plateau ages between 257 and 248 Ma. All the grains show partly disturbed ^{39}Ar releasing patterns with staircase shapes for the low-temperature steps, which is generally ascribed to radiogenic argon loss during post-crystallization fluid flow or brittle reactivation (e.g. Berger, 1975; McDougall and Harrison, 1999; Rolland et al., 2008; Sanchez et al., 2011; Tartèse et al., 2011; Lanari et al., 2014). As the temperature for brittle-ductile deformation in marbles (~200-300°C; e.g., Ashby and Verrall, 1978) is lower than the closure temperature of K-Ar system in phengite (>400°C, Villa, 1998), the ages obtained for these minerals are thus interpreted as ages for dynamic crystallization in the shear zone. All four age spectra from marble mylonite sample KG-14-29 phengites are consistent with a single crystallization event, bracketed, if we retain the two most meaningful plateau ages (aggregates 1 and 3), between 249 ± 1.7 and 248 ± 1.7 Ma. Thus, the phengite age range likely represents a single or several shearing events at 249-248 Ma, during south-directed thrusting on the NKTT. In regard to kinematics, this deformation is related to a N-S shortening phase involving the activity of several thrusts in the STS, including the Pobedi and the North Khan Tengri thrusts, in a global transpressional context (e.g., Jourdon et al., 2017; Fig. 9). Similar to slightly older ages (240–290 Ma) have been obtained by Konopelko et al. (2013) and Rolland et al. (2013) for dextral displacement of the TFF. Therefore, the tectonic context in the Middle-Late Permian is in agreement with a phase of N-S shortening + sinistral motion in

the STS coeval with dextral deformation along the TFF (Figs. 1, 9).

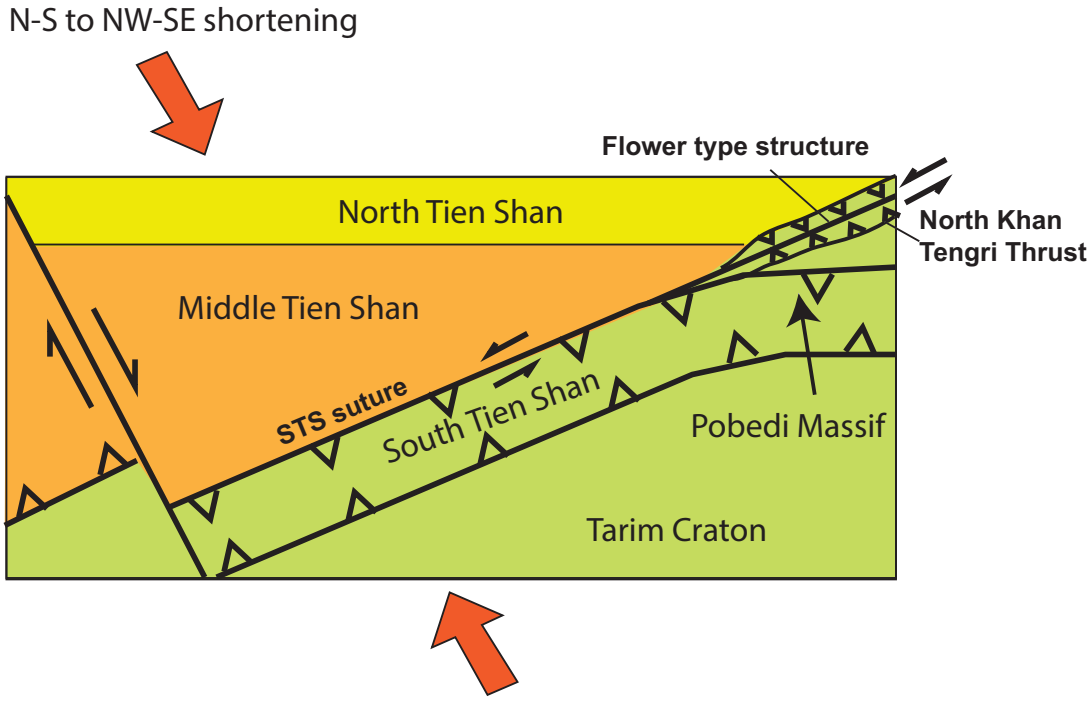

Fig. 9. Sketch of Tian Shan tectonic context at c. 260-240 Ma. Synchronous right-lateral motion of TFF and transpressional sinistral deformation along the South Tian Shan (STS) suggests a main N-S compression context. Middle Tian Shan (MTS) squeezes out towards the east in the eastern part of Kyrgyz STS close to the border with China. At this location, the termination of the MTS and the E-W strike of the STS give rise to a mainly compressional flower-type structure along the STS.

This tectonic phase directly followed a major phase of sinistral deformation along the STS, coeval with HT metamorphism and magmatism in the Early-Middle Permian at 287-265 Ma in the Pobedi Range and along strike in the Chinese STS (e.g., Loury et al., 2018a; Yu et al., 2017; Wali et al., 2017; Zhong et al., 2017). These main compressional shear zone phases occurred after 265 Ma, in agreement consistent with the $^{40}Ar/^{39}Ar$ age of 256–265 Ma obtained on biotites in the Pobedi HT unit (Loury et al., 2018a). $^{40}Ar/^{39}Ar$ ages obtained from amphiboles are similar to the U-Pb ages on zircon of 265-287 Ma in this unit, and thus represent the age of the metamorphic peak, while the biotite ages could be interpreted as a cooling age for the Pobedi HT unit (through ~300°C; Loury et al., 2018a). We thus propose that the N-S shortening phase is responsible for the exhumation of the HT Pobedi HT unit by the activation of the PT at a minimum age of 265 Ma. This compressional phase lasted until the Late Permian - Early Triassic, as shown by phengite $^{40}Ar/^{39}Ar$ ages of 248-249 Ma in the

North Khan Tengri Thrust, when a transpressive tectonic regime affected the entire study area (de Jong et al., 2009; Laurent-Charvet et al., 2003; Rolland et al., 2013; Konopleko et al., 2013). Such a fast cooling rate due to exhumation during transcurrent tectonics at that time is also described in the Chinese Tien-Shan and Altai along the Main-Tien-Shan and Erqishi shear zones (Laurent-Charvet et al., 2003). As shown by the Permian AHe ages of 260 ± 5 Ma (Fig. 7A), and similar ages obtained across the Tian Shan range (e.g., Glorie et al., 2019, and references therein), exhumation related to the transpressive tectonics lasted probably less than 10 Ma. Exhumation ended at c. 250 Ma, and deformation might have evolved as pure strike-slip with little exhumation in the Early Triassic until c. 240 Ma (Rolland et al., 2013; Konopelko et al., 2013).

4.2. Significance of the Permian – Early Cenozoic planation surface

Following the pioneering works of Afonichev and Vlasov (1984); Makarov (1977); Chediya (1986); Hendrix et al. (1992) and Dumitru et al. (2001) and more recent compilations of De Pelsmaeker et al. (2017), Chen et al. (2017), Jolivet et al. (2018), the planation surfaces developed through ongoing erosion during the Mesozoic in the entire western CAOB. Thermochronological data from the Song-Kul plateau, the Alai, Trans-Alai and Terskey ranges and from the central and western Chinese Tian Shan show slow basement cooling during most of the Jurassic (e.g. Dumitru et al., 2001; Sobel et al., 2006a; Jolivet et al., 2010; De Grave et al., 2011, 2012; Tang et al., 2015; Glorie and De Grave, 2016; Zhang et al., 2016; Gillespie et al., 2017a-b; Wang et al., 2017; Morin et al., 2019). The Permian-Cretaceous peneplain is recognized in the landscape in regions neighbouring the Pobedi range; therefore, in these areas, Cenozoic tectonics have resulted in surface uplift with very limited erosion. However, some slight differences in exhumation ages could reflect several tectonic phases, or a long lasting tectonic context punctuated by slight, distinct, along-belt exhumation episodes

543 during the Mesozoic (e.g., Jolivet, 2017). Permian-Triassic (280–210 Ma) titanite fission track
544 and zircon (U-Th)/He data (Glorie et al., 2011) along the southern margin of STS are
545 diagnostic of significant exhumation until the Triassic. In agreement with these data, we
546 document several AHe ages, which remained unreset in the Cenozoic, spanning 256-269 Ma
547 (sample KG-13-11) at Inylchek, to the west of the Pobedi-Khan Tengri massif. This age range
548 for the initial exhumation of the southern STS to a temperature <60°C (Ehlers and Farley,
549 2003) is in good agreement with the Late Permian tectonic phase evidenced by $^{40}Ar/^{39}Ar$
550 dating (see previous section 4.1.). As the AHe and $^{40}Ar/^{39}Ar$ ages overlap, this tectonic phase
551 is suggested to have resulted in rapid exhumation and vertical motions, which seemingly
552 stopped shortly after 250 Ma in that area. The Permian transpressional phase thus appears to
553 have been short-lived and laterally heterogeneous, and matches relatively well with the
554 ending of the Early to Middle Permian magmatic phase (~260 Ma; e.g. Wang et Liu, 1991;
555 Chen et al., 1999, 2009; Yang et al., 2006; Li et al., 2011; Yu et al., 2011; Biske et al., 2013;
556 Zhang et Zou, 2013b).
557 At the large scale, to the west, the neighbouring STS preserves some younger exhumation
558 ages. This article extends the work of Macaulay et al. (2014) and Glorie et al. (2011),
559 documenting a ~100-60 Ma planation surface preserved in the central Kyrgyz STS, to the
560 west of the Pobedi Massif, highlighted by Late Cretaceous (67-97 Ma) AHe ages in the Naryn
561 Valley and an age peak of ~ 63 Ma documented in the entire AHe dataset (Figs. 7-8 & Table
562 2). Similar Late Cretaceous / Early Cenozoic ages were also obtained in the Chinese TS to the
563 east (e.g., Jolivet, 2017) and reflect slow cooling at the scale of the STS. This age is rarely
564 documented in the Northern Tian Shan (De Grave et al. 2011), while it largely occurs within
565 the southern rim of CAOB (Gillespie et al., 2017a-b). SW of the Tian Shan in the South
566 Pamir, some authors propose that significant crustal thickening occurred in that time range

(Aminov et al., 2017), although there are still few direct constraints to tie Tian Shan exhumation to this Late Mesozoic tectonic event.

4.3. Respective parts of Permian and Cenozoic motions on major faults

Regarding the evolution of STS, a major question is how to estimate the relative contributions of Permian tectonics and Cenozoic structural reactivation to the net displacement of major faults? Direct and indirect constrains can be derived from geological analysis and thermochronology. (i) First, considering the Permian activity of the PT, the thrust places the hangingwall granulite facies unit on top of the footwall greenschist facies unit, which represents a significant metamorphic jump (Loury et al., 2018a). Cooling below 300°C of the hanging-wall compartment, constrained by biotite $^{40}Ar/^{39}Ar$ dating, occurred at 256-265 Ma. Given that high-temperature metamorphism in this hanging-wall is constrained at 6 kbar-850°C and is dated at 276.2 ± 2.0 Ma (Loury et al., 2018a), the maximum initial Permian offset of the PT should be > 8 km to explain its emplacement on top of the shallow footwall domain, with a geothermal gradient of 40°C.km^{-1}. In this paper, we obtain a peak of Permian AHe ages, which record exhumation of the PT footwall at 260.7±3.3 Ma (Fig. 7A). This age is in agreement with an exhumation of the STS following transpressional tectonics at 290-260 Ma (see discussions on the timing of collision in Loury et al., 2018b), after the termination of PT motion.

(ii) Considering the Cenozoic offset of the PT, we obtained partly reset/unreset AHe ages in the northern footwall part of the PT, while AHe ages were reset and lie within 8.3 ± 2.5 Ma in its southern hanging-wall part. We interpret this age difference as resulting from the Cenozoic top-to-the-north tectonic displacement of the PT. A ~60°C blocking temperature for the U-Th-Sm/He system in apatite (for a cooling rate of ~10° C/Ma; Reiners and Brandon, 2006), and a geotherm of 25°C/km for this period of time (Vinnik et al., 2004; Makarov et al., 2010;

593 Jourdon et al., 2018a), implies that 8.3 ± 2.5 Ma reflects the time of exhumation through a
594 depth of ~3 ± 0.5 km. The presence of Permian biotite $^{40}Ar/^{39}Ar$ ages shows that the
595 hanging-wall compartment was not subjected to temperatures above the cooling temperature
596 of biotite of ~300°C (Harrison et al., 1985) during the Cenozoic, corresponding currently to
597 an equivalent depth of ~12 km in the Tian Shan. Therefore, the Pobedi HT unit hanging wall
598 has experienced between ~3 and <12 km of Cenozoic exhumation. In the PT footwall domain,
599 Permian AHe ages from below the peneplain imply that the samples were exhumed close to
600 the earth surface at ~260-250 Ma, and were then buried to a depth equivalent to <60°C in the
601 Mesozoic-Cenozoic. Along strike to the east, at higher elevations in the PT footwall
602 compartment, Cenozoic reset AHe ages are found at an elevation of <3800 m, and, in this
603 domain a 7-8 Ma age would broadly correspond to an altitude of 2000-2500 m following the
604 age – elevation correlation (Fig. 7C). In this area, the maximum peak elevation is 5500 m.
605 This age pattern is in agreement with (i) little burial during the Cenozoic (less than 2-3 km, as
606 sediments were continuously removed from Tien Shan during thrusting (Jourdon et al.,
607 2018b), and (ii) with a minimum Cenozoic differential uplift of about 3 km (Vt in Fig. 7C),
608 and hence an approximate 4.2 km north-directed offset along the PT, given its 45° dip
609 towards the south (Fig. 7E). Since ~8.3 Ma, the average offset rate along this thrust would
610 thus be of about 0.3-0.7 mm/yr. This slip rate is much lower than those recorded on
611 'emblematic' collisional thrusts like the Main Central Thrust of Himalayas for instance (>10
612 mm/yr, e.g., Catlos et al., 2001).
613
614 *4.4. Out-of-sequence Late Miocene activation of deformation in the South Tian Shan*
615 In agreement with a previous compilation of thermochronological ages in the Kyrgyz Tian
616 Shan proposed by Macaulay et al. (2014), a north to south 'out-of-sequence' Cenozoic
617 deformation is suggested.

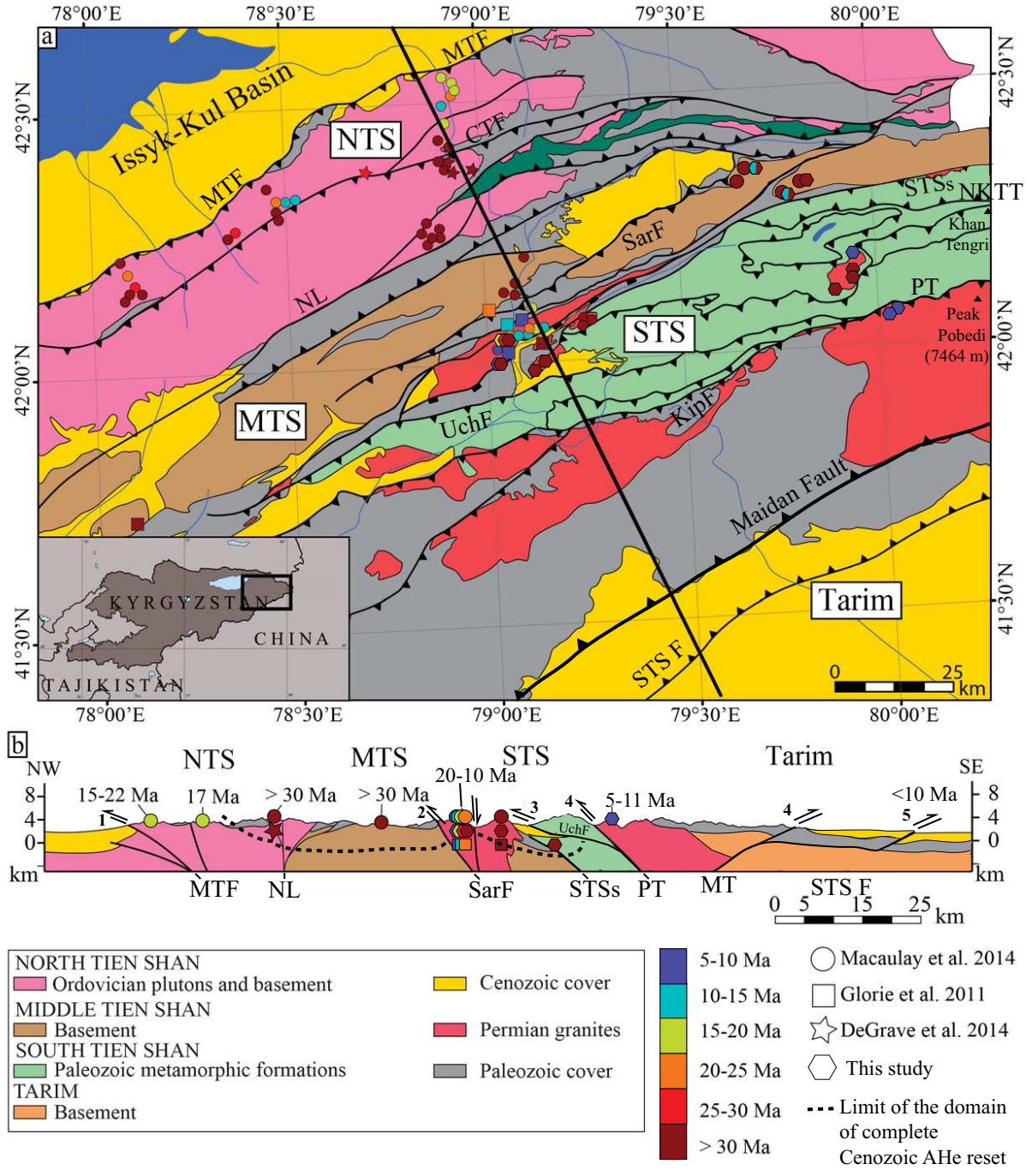

Fig. 10. A, Eastern Kyrgyz sketch geological map and compilation of main thermochronological results. B, Geological cross-section showing the major thrusts and their age of tectonic (re)activation during the Cenozoic. CTF: Central Terskey Fault; KipF: Kipchak Fault; MT: Maidan Thrust; MTF: Main Terskey Fault; NKTT: North Khan Tengri Thrust; NL: Nikolaev Line; PT: Pobedi Thrust; SarF: Sarajaz Fault; STS F: Southern Tian Shan Front; STSs: Southern Tian Shan Suture; UchF: Uchchat Fault.

Overall, the numerous AFT and FT ages compiled along the Issyk-Kul-Pobedi Massif transect (Fig. 10) highlight a top-to-the-north deformation event that likely started in the north (Main Terskey Fault, MTF) in the Late Oligocene-Early Miocene. Here, several points of evidence

suggest that the highest and southern part of the Tian Shan belt, the Pobedi Massif, was uplifted after the MTS, which argues for a progressive propagation of deformation in the belt towards the Tarim basin in the south (Figs. 10-11):

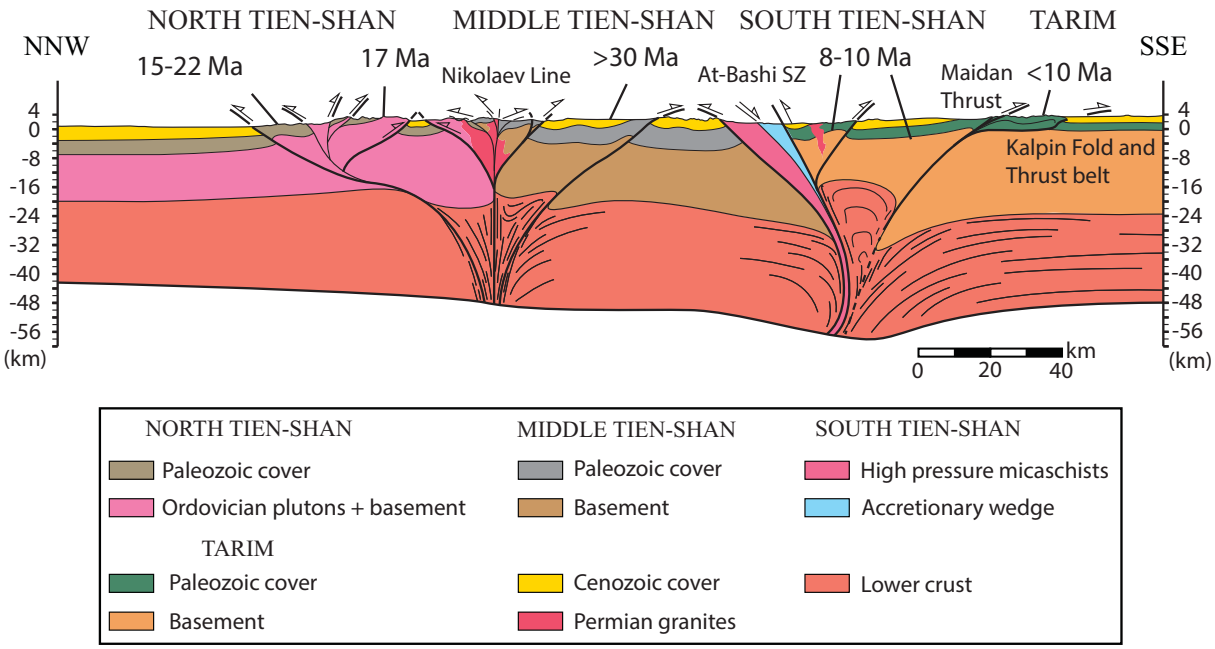

Fig. 11. Crustal-scale geological cross-section of the Kyrgyz-Chinese Tian Shan (79°E) after Jourdon et al. (2018b), showing the ages of the Cenozoic re-activation of major thrusts and their probable geometry at depth. The cross-section was built by coupling geological and geophysical data and numerical models (Jourdon et al., 2018b).

(i) At the scale of the Tian Shan belt, combined thermochronological data define a Cenozoic exhumation event starting at ca. 30 Ma (e.g., Bande et al., 2017 and references therein). The ages obtained by Macaulay et al. (2014) in the hanging wall of the MTF are within 15-22 Ma, which argues for Early-Middle Miocene activity of this fault. This event is correlated with synchronous tectonic activity along the TFF (Bande et al., 2017), implying that both strike-slip and north-directed thrust motions acted simultaneously at the onset of Cenozoic compressional deformation. In turn, these faults were synchronous with the Maidan and adjacent faults bounding Tarim (Heermance et al., 2008; Sobel et al., 2011). Therefore, the locus of deformation has shifted within the Tian Shan with an out-of-sequence style.

(ii) The ages obtained by Macaulay et al. (2014), Glorie et al. (2011) and this study for the hanging wall of the Sarajaz Fault, at the boundary between the Middle and North Tian Shan, mostly range between 20 and 5 Ma, which argues for its main activity during the Middle-Late Miocene. To the north of the Sarajaz Fault, the south NTS and MTS mostly preserve Mesozoic ages, and in any case ages older than 30 Ma, which is in good agreement with a north vergence for the Sarajaz Fault thrust and relative downthrow of this compartment.

(iii) The STS domain exhibits older, Permian ages (256-269 Ma, to the west at Inylchek) unreset during the Cenozoic, or variable partly reset ages (to the east between Khan Tengri and Pobedi peaks). This zone of older AFT ages is in agreement with a relative subsidence of that compartment accommodated by extensional displacement on the STS suture at the back of a possible anticline ramp structure.

(iv) The southern flank of the STS domain is uplifted by the top-to-the-north motion of the Uchchat and Kipchak faults, which merge into the PT (Figs. 2, 11). In this study, the new set of ages obtained in the high part of the Pobedi Massif suggest a Cenozoic reactivation of the PT after 10 Ma. This Late Miocene age for the PT reactivation is also supported by the geometry and polarity of the Aksu River drainage network (Fig. 8). This deeply incised, meandering river cuts across the high topography of the Pobedi Massif, flowing from north (MTS) to south (Tarim Basin), in agreement with a later uplift of the STS.

(v) The <10 Ma activation age of the PT is in good agreement with the net coeval increase in sedimentary rates documented in the north Tarim foreland basin all along the southern edge of the Tian Shan belt (e.g., Wu et al., 2019a-b; Chang et al., 2019; Jia et al., 2020). West to our study area, at the border with the Pamirs, a

673 marked increase in sedimentation rates at ~7 Ma, and a further rapid increase after
674 2.6 Ma, have been documented (Heermance et al., 2007; Chen et al., 2015; Qiao et
675 al., 2017; Liu et al., 2017). Similarily, to the south and east of our study area,
676 several studies show a marked increase in sedimentation rates after 20 Ma, and
677 especially between 12 and 5 Ma (Chang et al., 2012; 2017; Huang et al., 2006;
678 Charreau et al., 2006; Sun et al., 2009). These increased rates could be related to
679 the joint activation of the Pobedi and Maidan thrusts in a "flower-type" structure
680 (Figs. 10-11). Towards the south, the Maidan Thrust connects with a flat cover-
681 basement décollement, forming the Kalpin fold and thrust belt in the north Tarim
682 basin (e.g., Chang et al., 2019; Wu et al., 2019a-b; Figs. 10-11).

683 **Conclusions**

684 This study highlights two (Permian and Cenozoic) main phases of deformation related to the
685 activity and further reactivation of major thrusts within the STS: the Pobedi and the North
686 Khan Tengri Thrusts.

687 • $^{40}Ar/^{39}Ar$ dating of biotite and phengite at ca. 260-250 Ma agree with a maximum 12
688 km offset of the Pobedi Thrust and brittle-ductile deformation of the North Khan
689 Tengri Thrust.

690 • The AHe ages decrease from west to east. Towards the west, the importance of Late
691 Miocene uplift decreases sharply, while Late Permian exhumation ages (260-250 Ma)
692 are partly preserved below the Mesozoic unconformity at Inylchek, about 70 km to the
693 west of Pobedi Peak. In contrast, AHe ages obtained in the highest part of the massif,
694 in the Pobedi Thrust hangingwall highlight its Cenozoic re-activation at 8.3 ± 2.5 Ma,
695 with a differential uplift of 3 km along the thrust and a slip rate of 0.3-0.7 mm/yr.
696 Together with previous thermochronologic results from the Issyk-kul - Tarim transect,
697 these ages agree with a north to south 'out-of-sequence' thrust reactivation history,

which started about 20-30 Ma on several major faults such as the Main Terskey Fault in the north and the Maidan Fault in the south, and ended with the joint reactivation of the Pobedi Thrust and acceleration on the Maidan - STS frontal thrust.

Acknowledgements

This work was supported by the DARIUS programme and the ANR-DSP Tibet (ANR-13-BS06-012-01) supported by the Agence Nationale de la Recherche. The authors are indebted to Alexander Mikolaichuk and Dimtry Alexeiev for their assistance during field works and for fruitful discussions. This manuscript received useful and constructive feedback from Jian Chang and two anonymous reviewers.

References

Abdrakhmatov, K.Y., Aldazhanov, S.A., et al. 1996. Relatively recent construction of the Tian Shan inferred from GPS measurements of present-day crustal deformation rates. Nature 384, 450–453.

Alexeiev, D. V., Bykadorov, V. A., Volozh, Y. A., Sapozhnikov, R. B., 2017. Kinematic analysis of Jurassic grabens of soulthern Turgai and the role of the Mesozoic stage in the evolution of the Karatau–Talas–Ferghana strike-slip fault, Southern Kazakhstan and Tian Shan. Geotectonics 51(2), 105-120.

Aminov, J., Ding, L., Mamadjonov, Y., Dupont-Nivet, G., et al., 2017. Pamir Plateau formation and crustal thickening before the India-Asia collision inferred from dating and petrology of the 110–92 Ma Southern Pamir volcanic sequence. Gondwana Research 51, 310-326.

721 Arnaud, N. O., Kelley, S. P., 1995. Evidence for excess argon during high pressure
722 metamorphism in the Dora maira massif (Western Alps, Italy), using an ultra-violet laser
723 ablation microprobe ^{40}Ar-^{39}Ar technique. Contributions to Mineralogy and Petrology
724 121(1), 1-11.

725 Ashby, M. F., Verrall, R. A., 1978. Micro mechanisms of flow and fracture, and their
726 relevance to the rheology of the upper mantle. Philosophical Transactions of the Royal
727 Society of London, Series A 288, 59–95.

728 Afonichev, N. A., Vlasov, H. G., 1984. Geologischeskaya karta Kazakhstana i Sredney Azii
729 (so stratigraficheskimi kolonkami), Masshtab: 1:1,500,000 (Geological map of
730 Kazakhstan and Middle Asia (with stratigraphic columns), scale 1:1,500,000.

731 Bande, A., Sobel, E. R., Mikolaichuk, A., Acosta, V. T., 2017. Talas–Fergana Fault Cenozoic
732 timing of deformation and its relation to Pamir indentation. Geological Society, London,
733 Special Publications 427, SP427-1.

734 Biske, Y.S., Konopelko, D.L., Seltmann, R. 2013. Geodynamics of late Palaeozoic
735 magmatism in the Tian Shan and its framework. Geotectonics 47, 291–309.

736 Brown, R. W., Beucher, R., Roper, S., Persano, C., Stuart, F., Fitzgerald, P., 2013. Natural
737 age dispersion arising from the analysis of broken crystals: 1. Theoretical basis and
738 implications for the apatite (U-Th)/He thermochronometer. Geochim. Cosmochim. Acta
739 122, 478–497.

740 Bullen, M.E., Burbank, D.W., Garver, J.I. Abdrakhmatov, K.Y. 2001. Late Cenozoic tectonic
741 evolution of the northwestern Tian Shan: New age estimates for the initiation of
742 mountain building. Geological Society of America Bulletin 113, 1544–1559.

743 Bullen, M.E., Burbank, D.W., Garver, J.I., 2003. Building the Northern Tian Shan: Integrated
744 Thermal, Structural, and Topographic Constraints. The Journal of Geology 111, 149–165.

745 Carroll, A.R., Graham, S.A., Hendrix, M.S., Ying, D., Zhou, D., 1995. Late Palaeozoic
746 Tectonic Amalgamation of Northwestern China–Sedimentary Record of the Northern
747 Tarim, Northwestern Turpan, and Southern Junggar Basins. Geological Society of
748 America Bulletin 107, 571–594.

749 Catlos, E. J., Harrison, T. M., Kohn, M. J., Grove, M., Ryerson, F. J., Manning, C. E., Upreti,
750 B. N., 2001. Geochronologic and thermobarometric constraints on the evolution of the
751 Main Central Thrust, central Nepal Himalaya. Journal of Geophysical Research: Solid
752 Earth 106(B8), 16177-16204.

753 Chang, J., Qiu, N., Li, J. 2012. Tectono-thermal evolution of the northwestern edge of the
754 Tarim Basin in China: Constraints from apatite (U–Th)/He thermochronology. Journal of
755 Asian Earth Sciences 61, 187–198.

756 Chang, J., Tian, Y., Qiu, N., 2017. Mid-Late Miocene deformation of the northern Kuqa fold-
757 and-thrust belt (southern Chinese Tian Shan): An apatite (U-Th-Sm)/He study.
758 Tectonophysics, 694, 101-113.

759 Chang, J., Li, D., Min, K., Qiu, N., Xiao, Y., Wu, H., Liu, N., 2019. Cenozoic deformation of
760 the Kalpin fold-and-thrust belt, southern Chinese Tian Shan: New insights from low-T
761 thermochronology and sandbox modeling. Tectonophysics 766, 416-432.

762 Charreau, J., Gilder, S., et al. 2006. Magnetostratigraphy of the Yaha section, Tarim Basin
763 (China): 11 Ma acceleration in erosion and uplift of the Tian Shan Mountains. Geology
764 34, 181.

765 Chen, C., Lu, H., Jia, D., Cai, D., Wu, S. 1999. Closing history of the southern Tianshan
766 oceanic basin, western China: an oblique collisional orogeny. Tectonophysics 302, 23–
767 40.

768 Chen, H.L., Yang, S.F., Li, Z.L.Yu, X., Luo, J.C., He, G.Y., Lin, X.B., Wang, Q.H., 2009.
769 Spatial and temporal characteristics of Permian large igneous province in Tarim Basin (in
770 Chinese with English abstract). Petroleum Geology 30, 179–182.

771 Chen, X., Chen, H., Cheng, X., Shen, Z., Lin, X., 2015. Sedimentology and
772 magnetostratigraphy of the Tierekesazi Cenozoic section in the foreland region of south
773 West Tian Shan in Western China. Tectonophysics 654, 156-172.

774 Chen, Z., Wang, Z., Han, F., Zhang, W., Zhang, Q., et al., 2017. Late Cretaceous–Cenozoic
775 uplift, deformation, and erosion of the SW Tianshan Mountains in Kyrgyzstan and
776 Western China. International Geology Review 1-19.

777 De Grave, J., Buslov, M.M., Van den haute, P., 2007. Distant effects of India–Eurasia
778 convergence and Mesozoic intracontinental deformation in Central Asia: Constraints
779 from apatite fission-track thermochronology. Journal of Asian Earth Sciences 29, 188–
780 204.

781 De Grave, J., Glorie, S., et al. 2011. The thermo-tectonic history of the Song-Kul plateau,
782 Kyrgyz Tian Shan: Constraints by apatite and titanite thermochronometry and zircon
783 U/Pb dating. Gondwana Research 20, 745–763.

784 De Grave, J., Glorie, S., et al. 2012. Late Palaeozoic and Meso-Cenozoic tectonic evolution of
785 the southern Kyrgyz Tian Shan: Constraints from multi-method thermochronology in the

786 Trans-Alai, Turkestan-Alai segment and the southeastern Ferghana Basin. Journal of
787 Asian Earth Sciences 44, 149–168.

788 De Grave, J., Glorie, S., Buslov, M.M., Stockli, D.F., McWilliams, M.O., Batalev, V.Y., Van
789 den haute, P. 2013. Thermo-tectonic history of the Issyk-Kul basement (Kyrgyz Northern
790 Tian Shan, Central Asia). Gondwana Research 23, 998–1020.

791 De Grave, J., De Pelsmaeker, E., Zhimulev, F.I., Glorie, S., Buslov, M.M., Van den haute, P.,
792 2014. Meso-Cenozoic building of the northern Central Asian Orogenic Belt:
793 thermotectonic history of the Tuva region. Tectonophysics 621, 44-59.

794 De Jong, K., Wang, B.B., et al. 2009. New $^{40}Ar/^{39}Ar$ age constraints on the Late Palaeozoic
795 tectonic evolution of the western Tianshan (Xinjiang, northwestern China), with
796 emphasis on Permian fluid ingress. International Journal of Earth Sciences 98, 1239–
797 1258.

798 De Pelsmaeker, E., Jolivet, M., Laborde, A., Poujol, M., Robin, C., Zhimulev, F. I., et al.,
799 2017. Source-to-sink dynamics in the Kyrgyz Tian Shan from the Jurassic to the
800 Paleogene: Insights from sedimentological and detrital zircon U-Pb analyses. Gondwana
801 Research. Doi: 10.1016/j.gr.2017.09.004

802 Dobson, K. J., Stuart, F. M., Dempster, T. J., 2008. U and Th zonation in Fish Canyon Tuff
803 zircons: Implications for a zircon (U-Th)/He standard. Geochim. Cosmochim. Acta
804 72(19), 4745–4755.

805 Dumitru, T.A., Zhou, D., Chang, E.Z., Graham, S.A., Hendrix, M.S., Sobel, E.R. Carroll,
806 A.R., 2001. Uplift, exhumation, and deformation in the Chinese Tian Shan. Memoir -
807 Geological Society of America 194, 71–99.

808 Ehlers, T. A., Farley, K. A., 2003. Apatite (U-Th)/He thermochronometry: Methods and
809 applications to problems in tectonic and surface processes. Earth Planet. Sci. Lett. 206(1–
810 2), 1–14. doi:10.1016/S0012-821X(02)01069-5.

811 Farley, K. A., 2000. Helium diffusion from apatite: General behavior as illustrated by
812 Durango fluorapatite. Journal of Geophysical Research: Solid Earth 105(B2), 2903-2914.

813 Farley, K. A., 2002. (U-Th)/He dating; techniques, calibrations, and applications. Rev.
814 Mineral. Geochem. 47, 819–843.

815 Flowers, R. M., Ketcham, R. A., Shuster, D. L., Farley, K. A., 2009. Apatite (U–Th)/He
816 thermochronometry using a radiation damage accumulation and annealing model.
817 Geochimica et Cosmochimica acta 73(8), 2347-2365.

818 Fortuna, A.B., Kerimbekov, C.K., Mikolaichuk, A.V., 1994. Lithostratigraphic and
819 palynologic data of Cenozoic deposits of Tessik–Sarybulak depression. In: Geology of
820 Cenozoic and Seismotectonics of the Tian Shan (in Russian). Bishkek, Kyrgyzstan, pp.
821 26–39.

822 Gillespie, J., Glorie, S., Xiao, W., Zhang, Z., Collins, A. S., et al. 2017a. Mesozoic
823 reactivation of the Beishan, southern Central Asian Orogenic Belt: Insights from low-
824 temperature thermochronology. Gondwana Research 43, 107-122.

825 Gillespie, J., Glorie, S., Jepson, G., Zhang, Z. Y., Xiao, W. J., Danišík, M., Collins, A. S.,
826 2017b. Differential exhumation and crustal tilting in the easternmost Tianshan (Xinjiang,
827 China), revealed by low-temperature thermochronology. Tectonics 36(10), 2142-2158.

828 Glorie, S., De Grave, J., 2016. Exhuming the Meso-Cenozoic Kyrgyz Tienshan and Siberian
829 Altai-Sayan: a review based on low-temperature thermochronology. Geoscience Frontiers
830 7, 155-170.

831 Glorie, S., De Grave, J., Buslov, M.M., Elburg, M. A., Stockli, D.F., Gerdes, A. Van den
832 haute, P., 2010. Multi-method chronometric constraints on the evolution of the Northern
833 Kyrgyz Tian Shan granitoids (Central Asian Orogenic Belt): From emplacement to
834 exhumation. Journal of Asian Earth Sciences 38, 131–146.

835 Glorie, S., De Grave, J., et al. 2011. Tectonic history of the Kyrgyz South Tian Shan
836 (Atbashi-Inylchek) suture zone: The role of inherited structures during deformation-
837 propagation. Tectonics 30, TC6016.

838 Glorie, S., Otasevic, A., Gillespie, J., Jepson, G., Danišík, M., Zhimulev, F. I., et al., 2019.
839 Thermo-tectonic history of the Junggar Alatau within the Central Asian Orogenic Belt
840 (SE Kazakhstan, NW China): Insights from integrated apatite U/Pb, fission track and (U–
841 Th)/He thermochronology. Geoscience Frontiers 10(6), 2153-2166.

842 Han, B.F., He, G.Q., Wang, X.C., Guo, Z.J. 2011. Late Carboniferous collision between the
843 Tarim and Kazakhstan–Yili terranes in the western segment of the South Tian Shan
844 Orogen, Central Asia, and implications for the Northern Xinjiang, western China. Earth-
845 Science Reviews 109, 74–93.

846 Harrison, T. M., Duncan, I., McDougall, I., 1985. Diffusion of ^{40}Ar in biotite: temperature,
847 pressure and compositional effects. Geochimica et Cosmochimica Acta 49(11), 2461-
848 2468.

849 Heermance, R. V., Chen, J., Burbank, D.W., Miao, J., 2008. Temporal constraints and pulsed
850 Late Cenozoic deformation during the structural disruption of the active Kashi foreland,
851 northwest China. Tectonics 27, doi: 10.1029/2007TC002226.

852 Heermance, R. V., Chen, J., Burbank, D. W., Wang, C. S., 2007. Tectonic control on gravel
853 progradation and the significance of upward coarsening stratigraphy in the evolving
854 southwestern Chinese Tian Shan foreland. Basin Res. 19, 599 – 632. doi:10.1111/j.1365-
855 2117.2007.00339.x

856 Hegner, E., Klemd, R., et al. 2010. Mineral ages and P-T conditions of Late Palaeozoic high-
857 pressure eclogite and provenance of mélange sediments from Atbashi in the south
858 Tianshan orogen of Kyrgyzstan. American Journal of Science 310, 916–950.

859 Hendrix, M.S., 2000. Evolution of Mesozoic Sandstone Compositions, Southern Junggar,
860 Northern Tarim, and Western Turpan Basins, Northwest China: A Detrital Record of the
861 Ancestral Tian Shan. Journal of Sedimentary Research 70, 520–532.

862 Hendrix, M.S., Graham, S.A., Carroll, A.R., Sobel, E.R., McKnight, C.L., Schulein, B.J.,
863 Wang, Z., 1992. Sedimentary record and climatic implications of recurrent deformation
864 in the Tian Shan: Evidence from Mesozoic strata of the north Tarim, south Junggar, and
865 Turpan basins, northwest China. Geological Society of America Bulletin 104, 53–79.

866 Hendrix, M.S., Dumitru, T.A., Graham, S.A., 1994. Late Oligocene-Early Miocene unroofing
867 in the Chinese Tian Shan: An early effect of the India-Asia collision. Geology 22, 487.

868 Hu, X., Garzanti, E., Wang, J., Huang, W., An, W., Webb, A., 2016. The timing of India-Asia
869 collision onset–Facts, theories, controversies. Earth-Science Reviews 160, 264-299.

870 Huang, B.C., Piper, J.D.A., Peng, S.T., Liu, T., Li, Z., Wang, Q.C., Zhu, R.X., 2006.
871 Magnetostratigraphic study of the Kuche Depression, Tarim Basin, and Cenozoic uplift
872 of the Tian Shan Range, Western China. Earth Planet. Sci. Lett. 251, 346–364.

873 Jia, Y., Sun, J., Lü, L., 2020. Late Cenozoic tectono-geomorphologic evolution of the
874 northern Tian Shan mountain range: insight from U-Pb ages of detrital zircon grains from
875 the Upper Oligocene-Quaternary sediments of the southern Junggar Basin. Journal of
876 Asian Earth Sciences, 104286.

877 Jolivet, M., 2017. Mesozoic tectonic and topographic evolution of Central Asia and Tibet: a
878 preliminary synthesis. Geological Society, London, Special Publications 427(1), 19-55.

879 Jolivet, M., Ritz, J.-F., et al. 2007. Mongolian summits: An uplifted, flat, old but still
880 preserved erosion surface. Geology 35, 871.

881 Jolivet, M., De Boisgrollier, T., et al. 2009. How old is the Baikal rift zone? Insight from
882 apatite fission track thermochronology. Tectonics 28, doi: 10.1029/2008TC002404.

883 Jolivet, M., Dominguez, S., Charreau, J., Chen, Y., Li, Y., Wang, Q., 2010. Mesozoic and
884 Cenozoic tectonic history of the central Chinese Tian Shan: Reactivated tectonic
885 structures and active deformation. Tectonics 29, 1–30.

886 Jolivet, M., Bourquin, S., Heilbronn, G., Robin, C., Barrier, L., Dabard, M. P., ... Fu, B.,
887 2015. The Upper Jurassic–Lower Cretaceous alluvial-fan deposits of the Kalaza
888 Formation (Central Asia): tectonic pulse or increased aridity? Geological Society,
889 London, Special Publications 427, SP427-6.

890 Jolivet, M., Barrier, L., Dauteuil, O., Laborde, A., Li, Q., Reichenbacher, B., Guo, Z., 2018.
891 Late Cretaceous–Palaeogene topography of the Chinese Tian Shan: New insights from
892 geomorphology and sedimentology. Earth and Planetary Science Letters 499, 95-106.

893 Jourdon, A., Petit, C., Rolland, Y., Loury, C., Bellahsen, N., Guillot, S., et al. 2017. New
894 structural data on Late Palaeozoic tectonics in the Kyrgyz Tian Shan (Central Asian
895 Orogenic Belt). Gondwana Research 46, 57-78.

896 Jourdon, A., Le Pourhiet, L., Petit, C., Rolland, Y., 2018a. The deep structure and reactivation
897 of the Kyrgyz Tian Shan: Modelling the past to better constrain the present.
898 Tectonophysics 746, 530-548.

899 Jourdon, A., Le Pourhiet, L., Petit, C., Rolland, Y., 2018b. Impact of range-parallel sediment
900 transport on mountain building and exhumation in Kyrgyz Tian Shan. Terra Nova 30,
901 279-288.

902 Klemd, R., Bröcker, M., Hacker, B.R., Gao, J., Gans, P., Wemmer, K., 2005. New Age
903 Constraints on the Metamorphic Evolution of the High-Pressure / Low-Temperature Belt
904 in the Western Tianshan Mountains, NW China. The Journal of Geology 113, 157–168.

905 Konopelko, D., Biske, G., Seltmann, R., Eklund, O., Belyatsky, B., 2007. Hercynian post-
906 collisional A-type granites of the Kokshaal Range, Southern Tian Shan, Kyrgyzstan.
907 Lithos 97, 140–160.

908 Konopelko, D., Seltmann, R., Biske, G., Lepekhina, E., Sergeev, S., 2009. Possible source
909 dichotomy of contemporaneous post-collisional barren I-type versus tin-bearing A-type
910 granites, lying on opposite sides of the South Tian Shan suture. Ore Geology Reviews 35,
911 206–216.

912 Konopelko, D., Seltmann, R., Apayarov, F., Belousova, E., Izokh, A., Lepekhina, E., 2013.
913 U–Pb–Hf zircon study of two mylonitic granite complexes in the Talas-Fergana fault
914 zone, Kyrgyzstan, and Ar–Ar age of deformations along the fault. Journal of Asian Earth
915 Sciences 73, 334–346.

916 Kröner, A., Kovach, V., et al. 2014. Reassessment of continental growth during the
917 accretionary history of the Central Asian Orogenic Belt. Gondwana Research 25, 103–
918 125.

919 Kröner, A., Alexeiev, D. V., Kovach, V. P., Rojas-Agramonte, Y., et al., 2017. Zircon ages,
920 geochemistry and Nd isotopic systematics for the Palaeoproterozoic 2.3–1.8 Ga Kuilyu
921 Complex, East Kyrgyzstan–The oldest continental basement fragment in the Tianshan
922 orogenic belt. Journal of Asian Earth Sciences 135, 122-135.

923 Lanari, P., Rolland, Y., Schwartz, S., Vidal, O., Guillot, S., Tricart, P., Dumont, T. 2014. P-T-
924 t estimation of deformation in low-grade quartz-feldspar-bearing rocks using
925 thermodynamic modelling and 40 Ar/ 39 Ar dating techniques: example of the Plan-de-
926 Phasy shear zone unit (Briançonnais Zone, Western Alps). Terra Nova 26, 130–138.

927 Laurent-Charvet, S., Charvet, J., Monié, P., Shu, L., 2003. Late Palaeozoic strike-slip shear
928 zones in eastern Central Asia (NW China): New structural and geochronological data.
929 Tectonics 22(2), doi: 10.1029/2001TC901047.

930 Li, Z., Song, W., Peng, S., Wang, D., Zhang, Z. 2004. Mesozoic–Cenozoic tectonic
931 relationships between the Kuqa subbasin and Tian Shan, northwest China: constraints
932 from depositional records. Sedimentary Geology 172, 223–249.

933 Li, Q., Lin, W., Su, W., Li, X., Shi, Y., Liu, Y., Tang, G. 2011. SIMS U–Pb rutile age of low-
934 temperature eclogites from southwestern Chinese Tianshan, NW China. Lithos 122, 76–
935 86.

936 Lin, W., Faure, M., Nomade, S., Shang, Q., Renne, P.R. 2008. Permian–Triassic
937 amalgamation of Asia: Insights from Northeast China sutures and their place in the final
938 collision of North China and Siberia. Comptes Rendus Geoscience 340, 190–201.

939 Liu, D., Li, H., Sun, Z., Cao, Y., Wang, L., Pan, J., et al. 2017. Cenozoic episodic uplift and
940 kinematic evolution between the Pamir and Southwestern Tian Shan. Tectonophysics
941 712, 438-454.

942 Loury, C., Rolland, Y., Cenki-Tok, B., Lanari, P., Guillot, S., 2016. Late Palaeozoic evolution
943 of the South Tian Shan: Insights from P–T estimates and allanite geochronology on
944 retrogressed eclogites (Chatkal range, Kyrgyzstan). Journal of geodynamics 96, 62-80.

945 Loury, C., Rolland, Y., Guillot, S., Mikolaichuk, A. V., Lanari, P., Bruguier, O., Bosch, D.,
946 2017. Crustal-scale structure of South Tian Shan: implications for subduction polarity
947 and Cenozoic reactivation. Geological Society, London, Special Publications 427(1),
948 197-229.

949 Loury, C., Rolland, Y., Lanari, P., Guillot, S., Bosch, D., Ganino, C., Jourdon, A., Petit, C.,
950 Gallet, S., Monié, P., Riel, N., 2018a. Permian charnockites in the Pobedi area:
951 Implications for Tarim mantle plume activity and HT metamorphism in the South Tian
952 Shan range. Lithos 304, 135-154.

953 Loury, C., Rolland, Y., Guillot, S., Lanari, P., Ganino, C., et al., 2018b. Tectonometamorphic
954 evolution of the Atbashi high-P units (Kyrgyz CAOB, Tian Shan): Implications for the

closure of the Turkestan Ocean and continental subduction–exhumation of the South Kazakh continental margin. Journal of metamorphic geology 36(8), 959-985.

Macaulay, E.A., Sobel, E.R., Mikolaichuk, A., Landgraf, A., Kohn, B., Stuart, F., 2013. Thermochronologic insight into late Cenozoic deformation in the basement-cored Terskey Range, Kyrgyz Tian Shan. Tectonics 32, 487–500.

Macaulay, E.A., Sobel, E.R., Mikolaichuk, A., Kohn, B., Stuart, F. 2014. Cenozoic deformation and exhumation history of the Central Kyrgyz Tian Shan. Tectonics 33, 135–165.

Makarov, V.I., Alekseev, D. V., et al. 2010. Underthrusting of Tarim beneath the Tian Shan and deep structure of their junction zone: Main results of seismic experiment along MANAS Profile Kashgar-Song-Köl. Geotectonics 44, 102–126.

McDowell, F. W., McIntosh, W. C., Farley, K. A., 2005. A precise ^{40}Ar–^{39}Ar reference age for the Durango apatite (U–Th)/He and fissiontrack dating standard. Chem. Geol. 214, 249–263.

Metcalfe, I., 2013. Gondwana dispersion and Asian accretion: Tectonic and palaeogeographic evolution of eastern Tethys. Journal of Asian Earth Sciences, 66, 1–33.

Metelkin, D.V., Gordienko, I.V., Klimuk, V.S., 2007. Paleomagnetism of Upper Jurassic basalts from Transbaikalia: new data on the time of closure of the Mongol-Okhotsk Ocean and Mesozoic intraplate tectonics of Central Asia. Russian Geology and Geophysics 48, 825–834.

975 Min, K., Reiners, P. W., Wolff, J. A., Mundil, R., Winters, R. L., 2006. (U–Th)/He dating of
976 volcanic phenocrysts with high-U-Th inclusions Jemez Volcanic Field, New Mexico.
977 Chem. Geol. 227(3), 223–235. doi: 10.1016/j.chemgeo.2005.10.006

978 Molnar, P., Tapponnier, P., 2008. Cenozoic Tectonics of Asia: Effects of a Continental
979 Collision. Science 189, 419–426.

980 Morin, J., Jolivet, M., Barrier, L., Laborde, A., Li, H., Dauteuil, O., 2019. Planation surfaces
981 of the Tian Shan Range (Central Asia): Insight on several 100 million years of
982 topographic evolution. Journal of Asian Earth Sciences 177, 52-65.

983 Qiao, Q., Huang, B., Biggin, A. J., Piper, J. D., 2017. Late Cenozoic evolution in the Pamir-
984 Tian Shan convergence: New chronological constraints from the magnetostratigraphic
985 record of the southwestern Tianshan foreland basin (Ulugqat area). Tectonophysics 717,
986 51-64.

987 Reiners, P. W., Spell, T. L., Nicolescu, S., Zanetti, K. A., 2004. Zircon (U-Th)/He
988 thermochronometry: He diffusion and comparisons with $^{40}Ar/^{39}Ar$ dating. Geochim.
989 Cosmochim. Acta 68(8), 1857–1887.

990 Rizza, M., Abdrakhmatov, K., Walker, R., et al. 2019. Rate of slip from multiple Quaternary
991 dating methods and paleoseismic investigations along the Talas-Fergana Fault: tectonic
992 implications for the Tian Shan Range. Tectonics 38(7), 2477-2505.

993 Rolland, Y., 2002. From intra-oceanic convergence to post-collisional evolution: example of
994 the India-Asia convergence in NW Himalaya, from Cretaceous to present. Journal of the
995 Virtual Explorer 8, 185-208.

996 Rolland, Y., Pecher, A., Picard, C., 2000. Middle Cretaceous back-arc formation and arc
997 evolution along the Asian margin: the Shyok Suture Zone in northern Ladakh (NW
998 Himalaya). Tectonophysics 325(1), 145-173.

999 Rolland, Y., Alexeiev, D.V., Kröner, A., Corsini, M., Loury, C., Monié, P. 2013. Late
1000 Palaeozoic to Mesozoic kinematic history of Talas-Ferghana strike-slip Fault (Kyrgyz
1001 West Tianshan) revealed by a structural study and $^{40}Ar/^{39}Ar$ dating. Journal of Asian
1002 Earth Sciences 67-68, 76–92.

1003 Sanchez, G., Rolland, Y., Schneider, J., Corsini, M., Oliot, E., et al. 2011. Dating low-
1004 temperature deformation by $^{40}Ar/^{39}Ar$ on white mica, insights from the Argentera-
1005 Mercantour Massif (SW Alps). Lithos 125(1-2), 521-536.

1006 Sengör, A.M.C., Natalin, B.A., Burtman, V.S., 1993. Evolution of the Altaid tectonic collage
1007 and Palaeozoic crustal growth in Eurasia. Nature 364, 299–307.

1008 Shu, L., Charvet, J., Lingzhi, G., Lu, H., Laurent-Charvet, S., 1999. A Large-scale Palaeozoic
1009 Dextral Ductile Strike-Slip Zone: the Aqqikkudug-Weiya Zone along the Northern
1010 Margin of the Central Tianshan Belt, Xinjiang, NW China. Acta Geologica Sinica 73,
1011 148–162.

1012 Simon-Labric, T., Rolland, Y., Dumont, T., Heymes, T., Authemayou, C., Corsini, M.,
1013 Fornari, M., 2009. $^{40}Ar/^{39}Ar$ dating of Penninic Front tectonic displacement (W Alps)
1014 during the Lower Oligocene (31–34 Ma). Terra Nova 21(2), 127-136.

1015 Sobel, E.R., 1999. Basin analysis of the Jurassic–Lower Cretaceous southwest Tarim basin,
1016 northwest China. Geological Society of America Bulletin 111, 709–724.

1017 Sobel, E.R., Dumitru, T.A., 1997. Thrusting and exhumation around the margins of the
1018 western Tarim basin during the India-Asia collision. Journal of Geophysical Research
1019 102, 5043.

1020 Sobel, E.R., Oskin, M., Burbank, D. Mikolaichuk, A. 2006a. Exhumation of basement-cored
1021 uplifts: Example of the Kyrgyz Range quantified with apatite fission track
1022 thermochronology. Tectonics, 25, doi: 10.1029/2005TC001809.

1023 Sobel, E.R., Chen, J., Heermance, R. V. 2006b. Late Oligocene–Early Miocene initiation of
1024 shortening in the Southwestern Chinese Tian Shan: Implications for Neogene shortening
1025 rate variations. Earth and Planetary Science Letters 247, 70–81.

1026 Sobel, E. R., Schoenbohm, L. M., Chen, J., Thiede, R., Stockli, D. F., Sudo, M., Strecker, M.
1027 R., 2011. Late Miocene–Pliocene deceleration of dextral slip between Pamir and Tarim:
1028 Implications for Pamir orogenesis. Earth and Planetary Science Letters 304(3-4), 369-
1029 378.

1030 Steiger, R.H., Jager, E., 1977. Subcommission on geochronology: Convention on the use of
1031 decay constants in geo- and cosmochronology. Earth and Planetary Science Letters 36(3),
1032 359-362.

1033 Sun, J.M., Li, Y., Zhang, Z.Q., Fu, B.H., 2009. Magnetostratigraphic data on Neogene growth
1034 folding in the foreland basin of the southern Tianshan Mountains. Geology 37, 1051–
1035 1054.

1036 Tan, Z., Agard, P., Monié, P., et al. 2019. Architecture and PT-deformation-time evolution of
1037 the Chinese SW-Tianshan HP/UHP complex: Implications for subduction dynamics.
1038 Earth-Science Reviews 197, 102894.

1039 Tang, G. J., Wang, Q., Wyman, D. A., Sun, M., Li, Z. X., Zhao, Z. H., et al., 2010.
1040 Geochronology and geochemistry of Late Palaeozoic magmatic rocks in the Lamasu–
1041 Dabate area, northwestern Tianshan (west China): evidence for a tectonic transition from
1042 arc to post-collisional setting. Lithos 119(3), 393-411.

1043 Tursungaziev, B.T., Petrov, O.V. 2008. Geological map of Kirghyz republic, scale 1:500000
1044 (in russian). Saint-Petersburg VSEGEI.

1045 Vassallo, R., Jolivet, M., et al. 2007. Uplift age and rates of the Gurvan Bogd system (Gobi-
1046 Altay) by apatite fission track analysis. Earth and Planetary Science Letters 259, 333–
1047 346.

1048 Villa, I.M., 1998. Isotopic Closure. Terra Nova 10, 42–47.

1049 Vinnik, L.P., Reigber, C., Aleshin, I.M., Kosarev, G.L., Kaban, M.K., Oreshin, S.I., Roecker,
1050 S.W., 2004. Receiver function tomography of the central Tian Shan. Earth Planet. Sci.
1051 Lett. 225:131–146. http://dx.doi.org/10.1016/j.epsl.2004.05.039.

1052 Wali, G., Wang, B., Cluzel, D., Zhong, L., 2017. Carboniferous–Early Permian magmatic
1053 evolution of the Bogda Range (Xinjiang, NW China): Implications for the Late
1054 Palaeozoic accretionary tectonics of the SW Central Asian Orogenic Belt. Journal of
1055 Asian Earth Sciences 153, 238-251.

1056 Wang, B., Shu, L.S., Cluzel, D., Faure, M., Charvet, J., 2007. Geochemical constraints on
1057 Carboniferous volcanic rocks of the Yili Block (Xinjiang, NW China): Implication for
1058 the tectonic evolution of Western Tianshan. Journal of Asian Earth Sciences 29, 148–
1059 159.

1060 Wang, B., Cluzel, D., et al. 2009. Evolution of calc-alkaline to alkaline magmatism through
1061 Carboniferous convergence to Permian transcurrent tectonics, western Chinese Tianshan.
1062 International Journal of Earth Sciences 98, 1275–1298.

1063 Wang, B., Cluzel, D., et al. 2014. Late Palaeozoic pre- and syn-kinematic plutons of the
1064 Kangguer–Huangshan Shear zone: Inference on the tectonic evolution of the eastern
1065 Chinese north Tianshan. American Journal of Science 314, 43–79.

1066 Wang, Y., Cai, K., Sun, M., Xiao, W., De Grave, J., Wan, B., Bao, Z., 2017. Tracking the
1067 multi-stage exhumation history of the western Chinese Tianshan by apatite fission track
1068 (AFT) dating: Implication for the preservation of epithermal deposits in the ancient
1069 orogenic belt. Ore Geology Reviews. Doi: 10.1016/j.oregeorev.2017.04.011

1070 Windley, B.F., Alexeiev, D.V., Xiao, W., Kröner, A., Badarch, G., 2007. Tectonic models for
1071 accretion of the Central Asian Orogenic Belt. Journal of the Geological Society, London
1072 164, 31–47.

1073 Wu, C., Zheng, W., Zhang, P., Zhang, Z., Jia, Q., Yu, J., et al. 2019. Oblique thrust of the
1074 Maidan fault and late Quaternary tectonic deformation in the southwestern Tian Shan,
1075 Northwestern China. Tectonics 38(8), 2625-2645.

1076 Wu, C., Zheng, W., Zhang, Z., Jia, Q., Yang, H., 2019. Large-earthquake rupturing and
1077 slipping behavior along the range-front Maidan fault in the southern Tian Shan,
1078 northwestern China. Journal of Asian Earth Sciences, 104193.

1079 Yang, S., Chen, H., Jl, D., Li, Z., Dong, C., Jia, C., Wei, G. 2005. Geological process of early
1080 to middle Permian magmatism in Tarim Basin and its geodynamic significance (in
1081 Chinese). Geol Journal of China Universities 11, 504–511.

1082 Yang, S., Li, Z., Chen, H., Chen, W., Yu, X. 2006. ^{40}Ar-39Ar dating of basalts from Tarim
1083 Basin, NW China and its implication to a Permian thermal tectonic event. Journal of
1084 Zhejiang University Science A 7, 320–324.

1085 Yang, S.F., Li, Z.L., Chen, H.L., Santosh, M., Yu, X. 2007. Discovery of Permian bimodal
1086 dyke: Geochemistry and implications for tectonic evolution related to the last major
1087 tectono-thermal event in Tarim Basin, NW China. Gondwana Research 12, 113–120.

1088 Yang, Y. T., Guo, Z. X., Luo, Y. J., 2017. Middle-Late Jurassic tectonostratigraphic evolution
1089 of Central Asia, implications for the collision of the Karakoram-Lhasa Block with Asia.
1090 Earth-Science Reviews 166, 83-110.

1091 Yin, A., Harrison, T.M., 2000. Geologic evolution of the Himalayan-Tibetan orogen. Annual
1092 Review of Earth and Planetary Sciences 28, 211–280.

1093 Yin, A., Nie, S., Craig, P., Harrison, T.M., Ryerson, F.J., Xianglin, Q., Geng, Y., 1998. Late
1094 Cenozoic tectonic evolution of the southern Chinese Tian Shan. Tectonics 17, 1–27.

1095 Yin, J., Chen, W., Hodges, K. V., Xiao, W., Cai, K., et al., 2018. The thermal evolution of
1096 Chinese central Tianshan and its implications: Insights from multi-method chronometry.
1097 Tectonophysics 722, 536-548.

1098 Yu, X., Yang, S.-F., Chen, H.-L., Chen, Z.-Q., Li, Z.-L., Batt, G.E., Li, Y.-Q., 2011. Permian
1099 flood basalts from the Tarim Basin, Northwest China: SHRIMP zircon U–Pb dating and
1100 geochemical characteristics. Gondwana Research 20, 485–497.

1101 Yu, J., Li, N., Qi, N., Guo, J.P., Chen, Y.J., 2017. Carboniferous-Permian tectonic transition
1102 envisaged in two magmatic episodes at the Kuruer Cu-Au deposit, Western Tianshan
1103 (NW China), Journal of Asian Earth Sciences, doi: 10.1016/j.jseaes.2017.07.048.

1104 Zhang, B., Chen, W., Liu, J., Yin, J., Sun, J., 2019. Thermochronological insights into the
1105 intracontinental orogeny of the Chinese western Tianshan orogen. Journal of Asian Earth
1106 Sciences, 103927.

1107 Zhang, C.-L., Zou, H., 2013. Comparison between the Permian mafic dykes in Tarim and the
1108 western part of Central Asian Orogenic Belt (CAOB), NW China: Implications for two
1109 mantle domains of the Permian Tarim Large Igneous Province. Lithos 174, 15–27.

1110 Zhang, L., Ai, Y., et al. 2007. Triassic collision of western Tianshan orogenic belt, China:
1111 Evidence from SHRIMP U–Pb dating of zircon from HP/UHP eclogitic rocks. Lithos 96,
1112 266–280.

1113 Zhang, Y., Liu, J., Guo, Z. 2010. Permian basaltic rocks in the Tarim basin, NW China:
1114 Implications for plume–lithosphere interaction. Gondwana Research 18, 596–610.

1115 Zhang, Z., Zhu, W., Zheng, D., Zheng, B., Yang, W., 2016. Apatite fission track
1116 thermochronology in the Kuluketage and Aksu areas, NW China: implication for tectonic
1117 evolution of the northern Tarim. Geoscience Frontiers 7, 171-180.

1118 Zhao, S., Chen, W., Zhang, B., Sun, J., Shen, Z., Zhang, Y., 2019. Mesozoic and Cenozoic
1119 exhumation history and magmatic-hydrothermal events of the central Tianshan Mt.
1120 Range, NW China: Evidence from (U–Th)/He and $^{40}Ar/^{39}Ar$ dating. Journal of Asian
1121 Earth Sciences, 104057. https://doi.org/10.1016/j.jseaes.2019.104057

1122 Zhou, M.-F., Zhao, J.-H., Jiang, C.-Y., Gao, J.-F., Wang, W., Yang, S.-H., 2009. OIB-like,
1123 heterogeneous mantle sources of Permian basaltic magmatism in the western Tarim
1124 Basin, NW China: Implications for a possible Permian large igneous province. Lithos
1125 113, 583–594.

1126 Zhou, R., Schoennohm, L. M., Sobel, E. R., Davis, D. W., Glodny, J., 2017. New constraints
1127 on orogenic models of the southern Central Andean Plateau: Cenozoic basin evolution
1128 and bedrock exhumation. Geological Society of America Bulletin 129, 152–170. doi:
1129 10.1130/B31384.1

1130 Zhong, L., Wang, B., Alexeiev, D. V., Cao, Y., Biske, Y. S., Liu, H., et al., 2017. Palaeozoic
1131 multi-stage accretionary evolution of the SW Chinese Tianshan: New constraints from
1132 plutonic complex in the Nalati Range. Gondwana Research 45, 254-274.

Table 1. Sample KG1429 Mylonitic marble (KhanTengri area)

Step N°	36Ar(a) [fA]	37Ar(ca) [fA]	38Ar(cl) [fA]	39Ar(k) [fA]	40Ar(r) [fA]	Age (Ma)	± 1σ	40Ar(r) (%)	39Ar(k) (%)	Ca/K
Phengite aggregate 01 J = 0.00407000 ± 0.00002035 Age 249.53±1.70 Ma (MSWD = 1.44)										
1	0,58	115,6	0,10	1,1	20	130	± 87	10,5	0,33	0,004
2	0,06	102,8	-	0,4	6	96	± 270	41,9	-	-
3	0,03	68,4	-	0,3	4	91	± 419	58,1	-	-
4	0,25	91,7	0,05	9,6	292	211	± 14	79,5	2,85	0,045
5	0,18	85,2	-	5,0	155	216	± 19	74,5	-	-
6	0,09	503,3	0,03	3,4	169	338	± 39	119,6	1,00	0,003
7	0,34	93,9	0,04	20,5	729	245	± 4	87,7	6,08	0,094
8	0,07	139,7	0,06	13,0	474	251	± 7	96,1	3,85	0,040
9	0,10	3,3	0,07	38,2	1377	247	± 2	97,8	11,34	0,048
10	0,02	233,4	0,04	30,9	1149	255	± 4	100,6	9,16	0,057
11	0,03	10,9	0,01	23,8	868	250	± 4	99,1	7,06	0,941
12	0,12	48,8	0,06	53,7	1979	253	± 2	98,2	15,92	0,472
13	0,13	362,5	0,00	25,5	885	239	± 5	95,7	7,58	0,030
14	0,01	81,2	0,04	34,1	1249	251	± 3	99,8	10,13	0,181
15	0,08	221,2	0,00	23,2	820	243	± 6	97,1	6,87	0,045
16	0,10	227,0	0,09	44,7	1633	251	± 3	98,2	13,26	0,085
17	0,02	67,9	0,01	1,5	49	222	± 73	90,4	0,45	0,010
18	0,19	97,9	0,00	8,2	300	250	± 12	84,3	2,44	0,036
Phengite aggregate 02 J = 0.00407000 ± 0.00002035 Age 254.04±2.05 Ma (MSWD = 0.54)										
1	0,87	75,4	0,07	3,4	25	53	± 36	8,81	0,91	0,019
2	0,07	79,5	0,00	1,5	20	94	± 106	49,65	0,40	0,008
3	0,07	49,4	0,00	1,1	21	134	± 179	52,17	0,29	0,010
4	0,00	70,8	0,01	0,9	32	241	± 110	97,82	0,24	0,006
5	0,54	140,0	0,08	17,1	572	231	± 6	78,14	4,54	0,053
6	0,01	551,3	0,03	8,4	350	283	± 14	100,75	2,22	0,007
7	0,06	65,4	0,00	5,5	198	248	± 25	91,54	1,45	0,036
8	0,10	140,0	0,00	3,7	115	214	± 30	80,21	0,99	0,011
9	0,01	62,8	0,00	2,8	105	259	± 44	97,52	0,74	0,019
10	0,20	35,3	0,09	29,2	1033	243	± 5	94,46	7,74	0,356
11	0,10	119,2	0,03	22,6	798	243	± 5	96,40	6,00	0,082
12	0,02	170,9	0,05	16,9	630	256	± 6	100,77	4,47	0,042
13	0,04	40,0	0,00	12,2	435	246	± 9	97,61	3,22	0,131
14	0,05	123,4	0,09	58,1	2151	254	± 2	99,26	15,39	0,202
15	0,01	126,1	0,03	35,1	1306	255	± 3	99,66	9,29	0,120
16	0,05	87,2	0,11	63,9	2360	253	± 2	99,37	16,94	0,315
17	0,03	156,9	0,13	86,2	3219	256	± 1	99,66	22,85	0,236
18	0,01	21,1	0,02	5,4	207	261	± 26	99,05	1,44	0,111
19	0,03	182,6	0,09	3,3	149	304	± 32	94,18	0,88	0,008
Phengite aggregate 03 J = 0.00407000 ± 0.00002035 Age 248.02±1.74 Ma (MSWD = 1.45)										
1	0,02	400,1	0,22	3,0	60	144	± 35	92,58	1,11	0,003
2	0,06	259,9	0,09	1,3	46	247	± 80	155,66	0,48	0,002
3	0,08	300,3	0,05	0,0	30	-	-	627,35	0,00	0,000
4	0,19	77,9	0,15	13,2	415	218	± 10	87,82	4,93	0,073
5	0,18	129,1	0,03	7,3	247	232	± 16	82,01	2,75	0,024
6	0,11	136,9	0,00	5,0	166	231	± 22	83,57	1,85	0,016
7	0,25	175,7	0,25	24,6	903	252	± 2	92,35	9,20	0,060
8	0,18	406,1	0,13	18,0	629	240	± 2	92,36	6,75	0,019
9	0,24	458,9	0,31	54,8	1992	250	± 2	96,56	20,48	0,051
10	0,07	119,5	0,10	34,8	1267	250	± 2	98,34	13,03	0,125
11	0,10	299,2	0,00	17,2	591	237	± 5	95,43	6,43	0,025
12	0,11	288,7	0,00	38,4	1378	246	± 2	97,71	14,38	0,057
13	0,03	50,6	0,03	24,0	889	254	± 9	99,13	8,99	0,204
14	0,08	232,4	0,00	9,3	331	245	± 19	93,49	3,48	0,017
15	0,10	365,1	0,00	1,3	8	48	± 154	21,38	0,48	0,001
16	0,26	93,6	0,30	15,1	608	273	± 9	88,58	5,67	0,070
Phengite aggregate 4 J = 0.00407000 ± 0.00002035 Age 255.85±1.98 Ma (MSWD = 1.88)										
1	0,51	317,30	0,11	3,46	70,57	144	33	31,93	1,09	0,00
2	0,07	314,47	0,02	1,14	49,11	292	100	167,42	0,36	0,00
3	0,10	365,35	0,03	0,69	54,30	505	177	207,11	0,22	0,00
4	0,40	122,70	0,02	18,99	605,79	221	4	83,70	5,96	0,07
5	0,06	93,34	0,02	9,17	314,87	237	16	95,02	2,88	0,04
6	0,01	92,59	0,00	6,50	228,69	242	12	98,27	2,04	0,03
7	0,19	382,49	0,00	33,15	1118,38	233	5	95,30	10,40	0,04
8	0,15	418,69	0,00	22,10	728,21	228	5	94,09	6,94	0,02
9	0,17	327,61	0,04	73,08	2593,99	244	2	98,06	22,94	0,10
10	0,03	59,85	0,14	50,67	1850,71	251	2	99,53	15,90	0,36
11	0,09	187,17	0,09	38,89	1413,89	250	3	98,20	12,20	0,09
12	0,03	220,33	0,11	37,36	1419,64	260	4	100,51	11,73	0,07
13	0,06	150,85	0,01	11,71	456,97	267	10	96,16	3,67	0,03
14	0,03	110,71	0,00	2,08	76,51	252	48	89,20	0,65	0,01
15	0,15	48,59	0,00	5,89	249,84	288	19	84,61	1,85	0,05

Table 2. (U-Th-Sm)/He ages of Apatite (AHe) in the Pobedi Range (SE Kyrgyzstan).

Locality	Sample	Latitude (° ' ")	Longitude (° ' .)	Altitude (m)	AHe Age (Ma)[a]	2σ weighted error (Ma)	#t[b]	ESR (µm)	U (ppm)	Th (ppm)	147 Sm (ppm)	[U]e	Th/238 U	He (nmol/ g)	Ft
Naryntoo Range	KG-13-78-a	41 27 56.2	77 23 29,5	3634	97,2	1,9	1	44	26,8	52,7	16,3	39,2	2,0	13,7	0,66
Naryntoo Range	KG-13-78-b	41 27 56.2	77 23 29,5	3634	69,5	1,9	1	60	15,4	33,8	11,9	23,3	2,3	6,6	0,75
Naryntoo Range	KG-13-78-c	41 27 56.2	77 23 29,5	3634	67,2	0,8	1	75	10,8	26,9	8,0	17,1	2,6	5,0	0,80
Naryntoo Range	KG-13-78-d	41 27 56.2	77 23 29,5	3634	71,5	1,4	2	47	20,6	40,1	13,0	30,0	2,0	8,0	0,68
Naryntoo Range	KG-13-78-e	41 27 56.2	77 23 29,5	3634	85,5	2,1	1	51	12,8	18,0	5,7	17,0	1,5	5,6	0,71
W Pobeda Peak	KG-13-28b	42 02 43	79 57 44	5520	6,7	0,1	1	35	250,0	838,4	128,4	447,0	3,5	9,4	0,58
W Pobeda Peak	KG-13-28c	42 02 43	79 57 44	5520	10,6	0,1	1	46	193,9	239,6	87,5	250,2	1,3	9,7	0,67
W Pobeda Peak	KG-13-28d	42 02 43	79 57 44	5520	9,5	0,1	1	45	455,7	831,0	179,5	651,0	1,9	22,3	0,66
W Pobeda Peak	KG-13-28e	42 02 43	79 57 44	5520	10,1	0,2	1	47	133,3	181,3	51,4	175,9	1,4	6,5	0,68
W Pobeda Peak	KG-13-27-a	42 02 43	79 57 44	5530	7,0	0,2	0	58	258,4	577,1	130,7	394,0	2,3	11,1	0,74
W Pobeda Peak	KG-13-27-b	42 02 43	79 57 44	5530	6,0	0,1	1	55	206,4	610,9	186,0	350,0	3,1	8,3	0,73
W Pobeda Peak	KG-13-27-c	42 02 43	79 57 44	5530	7,1	0,2	1	54	115,8	596,1	210,2	255,9	5,3	7,2	0,72
W Pobeda Peak	KG-13-27-d	42 02 43	79 57 44	5530	12,5	0,3	2	63	65,0	257,1	106,4	125,4	4,1	6,6	0,76
W Pobeda Peak	KG-13-27-e	42 02 43	79 57 44	5530	5,2	0,3	1	56	25,9	31,8	46,4	33,4	1,3	0,7	0,73
Enylchek Glacier	KG-13-04a	42 08 18.3	79 57 05,3	3785	38,8	1,5	1	48	19,5	459,2	148,3	127,4	24,3	18,6	0,69
Enylchek Glacier	KG-13-04b	42 08 18.3	79 57 05,3	3785	30,3	1,5	1	53	2,0	9,2	56,9	4,2	4,7	0,5	0,72
Enylchek Glacier	KG-13-04c	42 08 18.3	79 57 05,3	3785	17,5	0,2	1	58	27,1	417,1	71,4	125,1	15,9	8,9	0,74
Enylchek Glacier	KG-13-04d	42 08 18.3	79 57 05,3	3785	19,6	0,4	1	66	15,8	25,3	57,9	21,7	1,7	1,8	0,77
Enylchek Glacier	KG-13-04e	42 08 18.3	79 57 05,3	3785	57,5	1,7	2	54	9,4	22,4	59,3	14,7	2,5	3,4	0,72
Enylchek Glacier	KG-13-04f	42 08 18.3	79 57 05,3	3785	8,6	0,3	1	55	41,2	407,2	111,8	136,9	10,2	4,7	0,73
Enylchek Glacier	KG-13-06c	42 06 44.7	79 56 08,8	4401	67,8	3,4	1	57	8,9	3,8	3,9	9,8	0,4	2,7	0,74
Enylchek Glacier	KG-13-06d	42 06 44.7	79 56 08,8	4401	291,0	13,7	2	66	0,1	4,3	3,6	1,1	42,5	1,4	0,77
Enylchek Glacier	KG-13-06e	42 06 44.7	79 56 08,8	4401	253,6	9,3	1	60	0,1	12,0	6,2	2,9	136,3	3,1	0,75
Enylchek Glacier	KG-13-32b	42 06 40.0	79 53 27,0	4625	277,4	41,0	1	63	0,0	0,2	0,0	0,1	7,3	0,1	0,76
Enylchek Glacier	KG-13-32e	42 06 40.0	79 53 27,0	4625	161,2	9,4	1	60	0,2	55,5	19,8	13,2	318,5	8,8	0,75
Enylchek Glacier	KG-13-11a	42 06 24.0	79 55 00,0	4750	86,4	6,5	2	56	0,1	4,4	0,5	1,2	36,1	0,4	0,73
Enylchek Glacier	KG-13-11c	42 06 24.0	79 55 00,0	4750	231,5	17,2	0	80	0,0	0,5	0,0	0,1	20,9	0,1	0,81
Enylchek Glacier	KG-13-11d	42 06 24.0	79 55 00,0	4750	62,3	15,1	0	65	0,1	0,5	0,0	0,2	5,3	0,1	0,77
Enylchek Mine	KG-13-39a	41 59 44.9	79 07 45,7	3566	257,0	6,8	1	67	4,4	16,7	65,4	8,3	3,9	9,7	0,78
Enylchek Mine	KG-13-39b	41 59 44.9	79 07 45,7	3566	*108,9*	2,5	0	57	23,4	106,8	141,4	48,5	4,7	21,7	0,74
Enylchek Mine	KG-13-39c	41 59 44.9	79 07 45,7	3566	*151,3*	5,1	0	65	4,2	17,3	63,8	8,3	4,2	5,6	0,77
Enylchek Mine	KG-13-39d	41 59 44.9	79 07 45,7	3566	268,9	6,9	1	59	8,8	40,7	67,1	18,3	4,8	20,7	0,74
Enylchek Mine	KG-13-39e	41 59 44.9	79 07 45,7	3566	256,1	5,7	1	53	40,6	232,8	199,2	95,3	5,9	97,5	0,72
Enylchek village (N)	KG-13-48-a	42 01 13.7	79 03 12,8	2486	4,6	0,2	1	43	103,6	7,0	44,5	105,3	0,1	1,7	0,65
Enylchek village (N)	KG-13-48-d	42 01 13.7	79 03 12,8	2486	76,2	2,0	1	48	20,5	33,3	12,4	28,3	1,7	8,1	0,69
Enylchek village (N)	KG-13-46a	42 01 31.5	79 02 15,4	2977	27,5	0,8	0	58	13,0	12,5	38,5	15,9	1,0	1,8	0,74
Enylchek village (N)	KG-13-46b	42 01 31.5	79 02 15,4	2977	62,5	1,3	0	62	5,7	11,2	35,0	8,3	2,0	2,2	0,76
Enylchek village (N)	KG-13-46c	42 01 31.5	79 02 15,4	2977	18,8	0,5	1	61	7,2	13,4	43,3	10,3	1,9	0,8	0,75
Enylchek village (N)	KG-13-46d	42 01 31.5	79 02 15,4	2977	63,3	1,2	2	65	22,0	13,0	45,9	25,1	0,6	6,7	0,77
Akchukkur	7TS302a	42 16 63.2	79 45 03,6	3818	159,9	2,1	2	51	6,5	21,6	27,0	11,6	3,4	7,3	0,71
Akchukkur	7TS302b	42 16 63.2	79 45 03,6	3818	13,6	0,3	0	57	14,9	54,1	47,2	27,6	3,8	1,5	0,74
Akchukkur	7TS302c	42 16 63.2	79 45 03,6	3818	55,0	0,8	1	62	6,5	22,7	27,6	11,9	3,6	2,7	0,76
Akchukkur	7TS302d	42 16 63.2	79 45 03,6	3818	62,8	1,0	2	53	10,2	39,1	39,8	19,4	3,9	4,8	0,72
Akchukkur	7TS305a	42 17 98.8	79 45 76,2	3540	62,1	1,6	1	62	3,9	8,0	4,6	5,8	2,1	1,5	0,76
Akchukkur	7TS305b	42 17 98.8	79 45 76,2	3540	73,0	2,2	1	70	3,8	4,1	2,9	4,7	1,1	1,5	0,79
Akchukkur	7TS305c	42 17 98.8	79 45 76,2	3540	35,7	1,1	2	66	3,5	5,8	3,5	4,9	1,7	0,7	0,77
Akchukkur	7TS305d	42 17 98.8	79 45 76,2	3540	110,1	3,6	1	59	2,6	10,0	6,5	5,0	3,9	2,3	0,74
Akchukkur	7TS305e	42 17 98.8	79 45 76,2	3540	27,8	0,7	1	69	2,8	7,4	4,7	4,6	2,7	0,5	0,78
Akchukkur	7TS307a	42 20 02.8	79 41 08,8	3202	13,1	1,7	2	70	1,1	0,2	0,1	1,2	0,2	0,1	0,79
Akchukkur	7TS307b	42 20 02.8	79 41 08,8	3202	53,2	1,7	2	53	3,1	1,9	0,8	3,6	0,6	0,7	0,72
Akchukkur	7TS307c	42 20 02.8	79 41 08,8	3202	59,2	2,3	2	60	1,2	1,8	1,9	1,6	1,6	0,4	0,75
Akchukkur	7TS307d	42 20 02.8	79 41 08,8	3202	16,1	1,0	2	74	1,1	0,5	0,1	1,2	0,4	0,1	0,80

[a]Ages are Ft corrected; [b]Terminations. In italic: discarded ages due to inconsistency and complex grain shape.

1134